

Deep indel mutagenesis reveals the regulatory and modulatory architecture of alternative exon splicing

Pablo Baeza-Centurion^{1,6*}, Belén Miñana^{2*}, Andre J. Faure¹, Mike Thompson¹, Sophie Bonnal², Gioia Quarantani^{1,3}, Ben Lehner^{1,3,4,5**}, Juan Valcárcel^{2,3,4**}

Affiliations

¹ Systems & Synthetic Biology Program, Centre for Genomic Regulation (CRG), The Barcelona Institute of Science and Technology, Dr Aiguader 88, Barcelona 08003, Spain

² Genome Biology Program, Centre for Genomic Regulation (CRG), The Barcelona Institute of Science and Technology, Dr Aiguader 88, Barcelona 08003, Spain

³ Universitat Pompeu Fabra (UPF), Barcelona 08003, Spain

⁴ Institució Catalana de Recerca i Estudis Avançats (ICREA), Pg. Lluís Companys 23, 08010 Barcelona, Spain

⁵ Wellcome Sanger Institute, Wellcome Genome Campus, Hinxton, UK

⁶ German Cancer Research Centre (DKFZ), Heidelberg, Germany

* These authors contributed equally to this work.

** These authors jointly supervised this work.

email: ben.lehner@crg.eu (BL), juan.valcarcel@crg.eu (JV)

33 Abstract

34
35 Altered splicing is a frequent mechanism by which genetic variants cause disease and
36 antisense oligonucleotides (AONs) that target pre-mRNA splicing have been approved as
37 therapeutics for multiple pathologies including patient-customized treatments for rare
38 diseases. However, the regulatory architecture of human exons remains poorly understood
39 and AON discovery is currently slow and expensive, limiting the wider adoption of the
40 approach. Here we show that that systematic deletion scans –which can be made
41 experimentally at very low cost – provide an efficient strategy to chart the regulatory landscape
42 of human exons and to rapidly identify effective splicing-modulating oligonucleotides in a fully
43 quantitative manner. Our results suggest a mechanism for the evolutionary origins of unusually
44 short microexons and the repression of transmembrane domain-encoding exons, and reveal
45 a checkerboard architecture of sequential enhancers and silencers in a model alternative
46 exon. Accurate prediction of the effects of deletions using deep learning provides a resource,
47 DANGO, that maps the splicing regulatory landscape of all human exons and predicts effective
48 splicing-altering antisense oligonucleotides genome-wide.
49
50
51

52 Introduction

53 Pre-mRNA splicing is the process by which introns are removed from transcripts and exons
54 are joined together to form mature mRNAs that are then exported to the cytoplasm and
55 translated¹. Altered splicing is an important mechanism by which genetic variants cause
56 disease²⁻⁴. Multiplex assays of variant effects (MAVEs) have revealed that random
57 nucleotide substitutions in exons frequently affect splicing, with 60-70% of substitutions in
58 over 90% of positions in alternatively-spliced exons⁵⁻⁷ and 5% of substitutions in
59 constitutively-spliced exons⁸ altering exon inclusion. Comprehensive testing has also shown
60 that ~10% of disease-causing missense variants, as well as 3% of common exonic
61 substitutions, affect splicing^{9,10}.

62
63 The impact of genetic variation beyond substitutions on splicing have been far less studied.
64 Insertions and deletions (indels)^{11,12} are abundant variants evident in 24% of Mendelian
65 diseases¹³, and disease-causing indels are enriched close to splice sites¹⁴. However, the
66 effects of indels on splicing have not been systematically tested.
67

68 The frequent disruption of splicing in human disease has led to extensive efforts to
69 therapeutically modulate splicing¹⁵. In particular, antisense oligonucleotides (AONs) that
70 modulate splicing have been approved as therapies for spinal muscular atrophy¹⁶ and
71 Duchenne muscular dystrophy¹⁷. Indeed AONs - because of their programmable sequence
72 specificity - may represent a general strategy to therapeutically modulate many splicing
73 changes¹⁸. However, predicting the impact of AONs on splicing is very challenging: AONs
74 need to be long to achieve sequence specificity (typically 18 to 21 nts) whereas splicing
75 regulatory elements are short and very poorly mapped genome-wide. Parameters that
76 influence AON efficacy include length, proximity to splice sites and binding energy¹⁹⁻²³. In
77 practice, however, identifying effective AONs requires laborious testing of many different
78 designs.
79

80 Here we use deep indel mutagenesis (DIM) to comprehensively quantify for the first time the
81 impact of all possible deletions and all small insertions on the splicing of a human exon, FAS
82 exon 6. Exon 6 encodes a transmembrane helix of the FAS/CD95 receptor. Inclusion of this
83 exon generates a pro-apoptotic receptor whereas exon skipping produces an anti-apoptotic
84 soluble inhibitor²⁴⁻²⁷. A variant in exon 6 that causes exon 6 skipping causes autoimmune
85 lymphoproliferative syndrome (ALPS)²⁸. Our data show that insertions and deletions
86 frequently disrupt splicing, with deletions in particular representing an efficient experimental
87 strategy to map the regulatory architecture of the exon. The deletion scan also defines the
88 minimum length of an exon and reveals a novel repressive regulatory mechanism whereby
89 cryptic sequences within an exon are recognised by a core component of the spliceosome
90 (U2 snRNP) that normally recognises intronic branch points. We show that this recognition of
91 cryptic exonic elements can be a mechanism for the evolutionary birth of unusually short
92 microexons²⁹. Using our data, we show that deep learning methods accurately predict the
93 effects of indels on splicing and that deletions accurately predict the splice-altering effects of
94 AONs. Finally, we provide a genome-wide resource, DANGO, that charts splicing regulatory
95 landscapes and splice-altering AONs across the human exome.
96

97 Results

98 Deep indel mutagenesis of a human alternatively spliced exon

99 To quantify in parallel how single nucleotide (nt) substitutions, deletions and insertions affect
100 alternative splicing of a human exon, we designed a library containing all single-nt
101 substitutions in the 63 nt-long FAS exon 6 ($n = 189$), as well as all deletions ranging in length
102 from 1 to 60 nts ($n = 2010$), all possible 1-, 2-, and 3-nt insertions ($n = 5208$), and a random
103 selection of 585 4-nt-long insertions (**figure 1A**). We cloned this library into a plasmid
104 minigene vector spanning FAS exons 5–7, transfected it into HEK293 cells, isolated RNA 48
105 h post-transfection and quantified the inclusion of each variant by counting how often it is
106 present in the final exon inclusion product compared to every other variant in the library by
107 deep sequencing of reverse transcription (RT)-PCR products (**figure 1B**). The resulting
108 enrichment scores allow the percent-spliced-in (PSI) value of each variant to be measured.
109 Our results were highly reproducible across nine experimental replicates (Pearson's r
110 between 0.97 and 0.98 for all pairs of replicates, **figure S1**) and our estimated PSI values
111 were very well correlated with PSI values determined by RT-PCR for 40 individual,
112 independently transfected, mutant minigenes, which included indel and substitution mutants
113 (Spearman's rho = 0.95, **figure 1C**).

114 The effects of single-nt substitutions, insertions and deletions 115 on exon inclusion

116 We quantified the effects of all single-nt substitutions ($n = 189$), insertions ($n = 187$) and
117 deletions ($n = 63$) on the inclusion of FAS exon 6 (**figure 1D-E**). The results revealed that
118 nearly the entire range of inclusion values can be obtained as a consequence of at least one
119 of the three classes of variant. Regardless of the type of mutation, just under two thirds
120 affected splicing by more than 10 PSI units (**figure 1D-E**): 61.9% of substitutions changed
121 the inclusion of FAS exon 6 by more than 10 PSI units (mean absolute Δ PSI = 17.5 PSI
122 units; consistent with previous data⁵), similar to 58.7% of single-nt deletions (mean absolute
123 Δ PSI = 15.5 PSI units) and 61.3% of single-nt insertions (mean absolute Δ PSI = 19.7 PSI
124 units).

125
126 Substitutions have a mode near the wild type (WT) PSI (49.1%) and they more often
127 promote skipping than inclusion, with 47.6% decreasing and 14.3% increasing inclusion by
128 more than 10 PSI units. Similarly, deletions tend to promote skipping, with 15.9% of single-nt
129 deletions promoting inclusion and 42.9% promoting skipping by more than 10 PSI units. In
130 contrast, insertions more frequently promote inclusion, with 41.1% increasing the inclusion of
131 FAS exon 6 and only 20.2% decreasing inclusion by more than 10 PSI units (**figure 1E**).
132

133 We next compared the effects of different mutation types in the same position along the
134 exon. The effects of single-nt substitutions and deletions in the same positions correlate
135 moderately well (Spearman's rho = 0.46, **figure 1F**), consistent with some of these variants
136 disrupting existing regulatory elements and with positive regulatory elements covering a
137 larger proportion of the exon than negative elements (**figure 1D-E**). However, the effects of
138 substitutions and deletions correlate poorly with the effects of insertions before or after the

139 substituted/deleted position (**figure 1G-H**, **figure S2**, **figure S3**). This suggests that
140 insertions often affect splicing by a different mechanism, for example by the creation of new
141 regulatory sequences (see below).

142 The effects of short multi-nt deletions and insertions on exon 143 inclusion

144 We next analysed the influence of short multi-nt deletions (ranging from 2 to 9 nts) and
145 insertions (either 2,3 or 4 nts) on exon inclusion. Short multi-nt deletions had a similar effect
146 on exon inclusion as single-nt deletions. Thus, 64.5% of 2-nt deletions affected splicing by
147 more than 10 PSI units (mean absolute Δ PSI = 17.0), as well as 62.3% of 3-nt deletions
148 (mean absolute Δ PSI = 17.9) and 73.3% of 4-nt deletions (mean absolute Δ PSI = 20.8).
149 Considering all short deletions up to 10 nts long, 66.0% altered inclusion by more than 10
150 PSI units (mean absolute Δ PSI = 18.7). Short multi-nt deletions longer than 2nt more
151 frequently promote skipping, with 30.6% of 2-nt deletions, 39.3% of 3-nt deletions, 43.3% of
152 4-nt deletions and 45.8% of all deletions spanning 10 or fewer nts decreasing exon inclusion
153 by more than 10 PSI units. In contrast, 33.9% of 2-nt deletions, 23.0% of 3-nt deletions, 30%
154 of 4-nt deletions and 20.2% of all deletions up to 10 nts long increase inclusion by more than
155 10 PSI units.

156

157 Longer multi-nt deletions are particularly effective at revealing splicing regulatory elements
158 (**figure 2A**). Thus, while 1-4 nt deletions at the 5' end of the exon showed multiple,
159 seemingly contradictory effects, longer deletions delineated ~8 5' terminal nts whose
160 collective deletion strongly promotes exon skipping. Similarly, deletions that cover exon
161 positions 9 to 18 consistently increase exon inclusion. Interestingly, deletions that partially
162 overlap this region (on either side) have the inverse effect and promote exon skipping.
163 Systematic deletion scans thus delineate consistent discrete regulatory elements (enhancers
164 and silencers), often adjacent to each other, and reveal patterns such as alternating
165 elements with antagonistic effects (**figure 2A**).

166

167 Short multi-nt insertions had a stronger effect on FAS exon 6 inclusion compared to single-nt
168 insertions. Thus, 74.5% of 2-nt insertions and 77.5% of 3-nt insertions changed inclusion by
169 more than 10 PSI units (mean absolute Δ PSI = 23.9 and Δ PSI = 24.2, respectively). Our
170 library also contained a random selection of 585 4-nt insertions, of which 88.6% changed
171 splicing by more than 10 PSI units (mean absolute Δ PSI = 31.2). Similar to single-nt
172 insertions, but in contrast with short multi-nt deletions, short multi-nt insertions tended to
173 promote inclusion rather than skipping: 44.6% of 2-nt insertions increased exon inclusion by
174 more than 10 PSI units (compared to 30.0% which decreased inclusion by this same
175 amount), as well as 42.4% of 3-nt insertions (35.1% for skipping) and 57.5% of 4-nt
176 insertions (31.2% for skipping).

177

178 In contrast to the regulatory landscape emerging from deletion analyses (**figure 2A**), double
179 or triple nt insertions tended to show autonomous effects that were strongly influenced by
180 the nature of the inserted nts (**figure 2B-C**, **figure S4**). Thus, insertion of GC, CG or GA
181 dinucleotides resulted in general increases in exon inclusion, almost independently of the
182 position of the insertion, with the prominent exception of the exon 3' end. In contrast,
183 insertion of GG or CC showed markedly different effects depending on the site of insertion.

184
185 The effects of triple nt insertions were even more idiosyncratic (**figure 2C**). For example, all
186 CG-containing triplets enhanced exon inclusion in nearly all positions (as was the case of
187 GC, CG or GA dinucleotides), with the notable exception of the five 3' nts of the exon.
188 Almost any insertion in this region (except those positioning an A at the 3' end of the exon)
189 led to enhanced exon skipping (black vertical rectangles on the right of panels **2B-C**),
190 suggesting that it harbours a strong enhancer sequence very sensitive to insertions or
191 deletions, possibly important for activation of the adjacent 5' splice site. Effects similar to
192 those of CG-containing triplets were observed upon insertion of a variety of GC / GA / GG-
193 containing triplets (lower rows of **figure 2C**); some of these effects might be related to
194 enrichment in purine residues which, together with other purines present in the insertion site,
195 could function as purine-rich exonic enhancers, a well-known class of exonic regulatory
196 elements³⁰. Indeed, these effects are also observed for other purine-rich triplets such as
197 GAG or AAG, albeit not for all (e.g. AGG or GGG). Triplets containing AU/UA dinucleotides
198 (e.g. UAG, UAA, UUA, AUU, CUA) promote skipping when inserted at most exonic positions
199 (cluster of blue colour in mid-low rows of panel **2C**), which might be explained by enhanced
200 binding of hnRNP proteins such as hnRNP A1³¹, which are known to mediate effects of
201 exonic silencers³². Pyrimidine-rich triplets (e.g. UCC, UUC, CUU), which could
202 provide/reinforce binding sites for other repressive hnRNPs such as PTB/hnRNP I, have
203 however very regional effects, promoting skipping mainly in already pyrimidine-rich regions
204 like the previously described PTB silencer located in positions 28-39 (middle upper black
205 rectangle in panel **2C**). A variety of cytosine-containing triplets systematically promote
206 inclusion when introduced between exon positions 17-24 (upper left black rectangle in panel
207 **2C**), which is a G-rich sequence, while insertion of 3 additional Gs in this region strongly
208 inhibits inclusion, suggesting that a G-rich silencer in this region, possibly forming G-
209 quadruplexes recognized by hnRNP F/H factors³³, is disrupted by C-containing triplets. The
210 latter effects could be in part linked to the creation of CG dinucleotides, which as discussed
211 above display strong enhancing effects.
212
213 We next evaluated the extent to which the effects of 2- and 3-nt insertions in FAS exon 6
214 predict the association between 2- and 3-nt kmer content and exon inclusion transcriptome-
215 wide. Strikingly, there is a strong positive correlation (Spearman's rho between 0.72 and
216 0.87 for 2-mers, between 0.69 and 0.79 for 3-mers) between the Δ PSI induced by kmer
217 insertions in our library and the PSI of exons containing at least 20 (for 2-mers) or 10 (for 3-
218 mers) such kmers in the GTEx database, either in adipose tissue (**figure 2D**) or in all GTEx
219 tissues (**figure S5**). Furthermore, the relationship between the content of each individual
220 nucleotide in the inserted 3-mers and the PSI of the mutated exon (**figure 2E**) resembles the
221 relationship between the content of each individual nucleotide in cassette exons and their
222 PSI (**figure 2F**). For example, increasing the number of uridines in an inserted triplet
223 correlates with increased exon skipping (**figure 2E**), similarly to how a larger uridine content
224 is associated with increased skipping in exons throughout the genome (results for GTEx
225 adipose tissue are shown in **figure 2F**, results for all GTEx tissues are shown in **figures S6-S9**).
226 These results argue that the effects of systematic analysis of insertion mutations
227 observed in our experiment for one individual model exon have captured sequence features
228 relevant for the inclusion of alternatively-spliced exons genome-wide.

229 Systematic deletion scans reveal the checkerboard regulatory 230 landscape of a human exon

231 Deletions are more likely to cause loss-of-function molecular effects than insertions that are
232 more likely to create new regulatory elements. Plotting the effects on inclusion of all possible
233 deletions from size 1 to 60 nts provides a comprehensive deletion map of FAS exon 6
234 (**figure 5B**, bottom triangle). The map reveals several regions whose deletion leads to
235 enhanced inclusion (exonic silencers, red areas) or enhanced skipping (exonic enhancers,
236 more green areas), arranged in an alternating 'checkerboard' pattern and covering most of
237 the exon length. These regulatory elements can also be visualised by plotting the effects on
238 exon inclusion of 1 to 6 nt-long deletions versus the position of the deletion along the exon
239 (**figure 5C**, left panel) and using local polynomial regression (LOESS) to identify sequence
240 'blocks' where deletions promote more inclusion or more skipping. These regulatory blocks
241 recapitulate well-known regulatory elements in FAS exon 6, namely EWS binding exonic
242 enhancers at positions 15-23 and 55-63³⁴, a PTB-binding silencer in positions 25-40³⁵, and
243 an SRSF6 enhancer at positions 40-45³⁶, as well as other elements that have not been fully
244 characterised to date, in particular a very active silencer located between positions 8 and 13.
245 Interestingly, deletions affecting nt C33 show different effects compared to deletions
246 affecting only its flanking nts, and these differential effects are consistent across a wide
247 range of deletion mutant lengths (blue square in the lower middle part of panel **5B**). Mutation
248 of C33 has been reported to cause FAS exon 6 skipping in patients with ALPS²⁸ and our
249 deletion scans further emphasise the particular effects of deletions containing this
250 nucleotide, demarcating a splicing enhancer embedded within two silencers previously
251 associated with PTB-mediated repression³⁵. Finally, a general observation is that deletions
252 above a certain length tend to induce strong skipping (lower left triangle in panel **5B**),
253 defining the exon length below which exon definition is likely failing (40 – 50 nts)^{37,38} (but see
254 below).

255

256 Collectively, our results suggest that systematic deletion mutagenesis is a particularly
257 informative experimental design to rapidly identify splicing regulatory elements throughout an
258 exon.

259 Small insertions create novel microexons by activating cryptic 260 splice sites within FAS exon 6

261 We next analysed the relationship between exon length and inclusion in our library.
262 Specifically, we asked, at 1 nt resolution, how short an exon can be while still being
263 recognised by the splicing machinery. There is no clear dependence of exon inclusion on
264 length for exons longer than 50 nts (up to 13 nt-long deletions). Then, inclusion gradually
265 decreases with increasing deletion length (i.e. shorter exons are less included), with almost
266 no exons shorter than 30 nts showing detectable levels of inclusion in our library (**figure 3A**).
267 Consistent with this – and previous large deletions in constitutive exons³⁷⁻³⁹ – exons shorter
268 than 30 nts are more likely to be skipped genome-wide compared to longer exons (results
269 for GTEx adipose tissue are shown in **figure 3B**, results for all GTEx tissues are shown in
270 **figure S10**).
271

272 Exons shorter than 27 nts are detected in multicellular animal but are categorised as a
273 special class - microexons - whose recognition requires a dedicated set of regulatory
274 sequences and factors (such as SRRM3/4) that enable their inclusion in specific tissues (e.g.
275 the brain or endocrine pancreas^{40,41}). However, we observed that a group of very short
276 exons (microexons, length-wise) from our library were detectably included (**figure 3A**).
277 These microexons appeared to correspond to large deletions at the 5' or 3' ends of FAS
278 exon 6 (**figure S11A**). However, these deletion mutants showed no evidence of exon
279 inclusion when tested individually (**figure S11B**). We realised that these apparently
280 contradictory results could be explained if the clones detected by deep sequencing of the
281 exon inclusion amplicon product were not the result of splicing of very short exons flanked by
282 FAS exon 6 splice sites, but rather result from the use of cryptic splice sites within exon 6
283 that have been activated by another mutation that is no longer present in the spliced-in exon
284 sequence. The central part of FAS exon 6 (positions 24 – 40) contains a pyrimidine-rich tract
285 that resembles the polypyrimidine (Py)-tracts that precede 3' splice sites, and nts in positions
286 10-15 contain a sequence that - strikingly - matches a branch point sequence⁴² (**figure 3C**).
287 We reasoned that, if an AG-containing kmer were to be introduced after the pyrimidine (Py)-
288 rich segment, this would result in a 3' splice site-like sequence arrangement that, if
289 recognised by the spliceosome, could create a novel microexon spanning from this new 3'
290 splice site to the 3' end of exon 6 (**figure 3D**). To test this possibility, we inserted AG-
291 creating triplets (like CAG or CUA -as the next nt is a G-) after the Py-tract in the FAS exon 6
292 minigene and observed that exons corresponding to the final part of the exon were included
293 to some extent in the mature RNA (**figure 3E**). In contrast, insertion of GAC, that does not
294 create a 3' splice site, does not result in activation of a shorter exon, but rather enhances the
295 inclusion of its full-length version (**figure 3E**).
296

297 Interestingly, the exonic Py-tract is longer and more uridine-rich than the Py-tract associated
298 with the natural 3' splice site of intron 5 (**figure 3C**). To assess whether the interplay
299 between these 3' splice sites plays a role in regulation, we strengthened the Py-tract of the
300 natural 3' splice site (**figure 3F**). In the presence of this mutation, inclusion of the full-length
301 exon was enhanced in the wild type minigene and activation of the cryptic 3' splice site in the
302 AG-containing construct was greatly reduced (**figure 3G**).
303

304 Previous work showed that the pyrimidine-rich sequence within FAS exon 6 functions as a
305 silencer when bound by PTB⁴³ (**figure 3H**). As expected, overexpression of PTB led to
306 skipping of the wild type exon (**figure 3I**, left panel) and also to reduced inclusion of the
307 shorter exon in the AG-containing construct (**figure 3I**, right panel), most likely due to direct
308 competition between PTB and the Py-tract-binding splicing factor U2AF^{43,44}. Finally, we
309 tested whether over-expression of SRRM4, which triggers inclusion of microexons in
310 neurons⁴⁰, has any effect on inclusion of the shorter version of FAS exon 6 (**figure 3J**).
311 Surprisingly, SRRM4 overexpression enhanced inclusion of the shorter exon (**figure 3K**)
312 despite this exon not being flanked by *cis*-acting sequences typically required for the
313 inclusion of microexons (e.g. intronic UGC motifs⁴⁵). Interestingly, SRRM4 reduced, rather
314 than enhanced, inclusion of the wild type full length exon 6 (**figure 3K**). These results show
315 that the short exon activated by a cryptic 3' splice site in exon 6 is not only recognized by the
316 splicing machinery but can be subject to splicing regulation by mechanisms similar to those
317 operating on natural microexons.
318

319 Our results thus far do not account for the detection of short exons spanning the first third of
320 FAS exon 6 (**figure 3C**). However, inserting sequences that mimic a 5' splice site (e.g. UAA)
321 after exon positions 18 or 19 induced the accumulation of spliced products containing these
322 sequences (**figure S11C**). Interestingly, the Py-tract in the central region of FAS exon 6 is
323 similar to a Py-tract found downstream of FAS exon 6 5' splice site (**figure 3C**), which is
324 recognized by the protein TIA1 and enhances 5' splice site recognition by U1 snRNP^{35,46}.
325 The Py-tract in the central region of FAS exon 6 could therefore enhance recognition of
326 upstream 5' splice sites generated by exonic mutations.
327
328 These findings reveal that FAS exon 6 contains 3' and 5'-like sequences that can be
329 activated by simple mutations to function as *bona fide* splice sites, promoting the inclusion of
330 very short exons even in the absence of regulatory sequence elements known to be involved
331 in the activation of microexons. The evolutionary birth of new microexons is therefore likely
332 to be simpler and more frequent than previously appreciated.

333 Exonic binding of U2 snRNP promotes FAS exon 6 skipping

334 The presence of a relatively strong Py-tract preceded by a near-consensus branch point
335 sequence within exon 6 (**figure 3C**), and the inclusion of a shorter version of the exon when
336 a mutation creates a functional 3' splice site AG downstream of the Py-tract, opened the
337 possibility that 3' splice site recognizing factors assemble on FAS exon 6 (**figure 3L-M**).
338

339 To directly assess whether U2 snRNP, the key ribonucleoprotein complex involved 3' splice
340 site recognition, can assemble on FAS exon 6 sequences, we incubated *in vitro* transcribed
341 FAS exon 6 (wild type and mutants, all lacking the flanking splice sites) with HeLa nuclear
342 extracts and measured the interaction by native gel electrophoresis. The results indicated
343 that U2 snRNP can indeed assemble (complex A) on FAS exon 6, an interaction that was
344 decreased upon mutation of the Py-tract or branch point sequences and enhanced upon
345 introduction of an AG dinucleotide (**figure 3L-M** and **figure S12**).
346

347 It is conceivable that U2 snRNP assembly on the wild type exon, in the absence of a 3'
348 splice site, competes with recognition of the 3' splice site of intron 5 by the splicing
349 machinery and this contributes to modulate the levels of exon 6 inclusion. To test this
350 possible mechanism, we took advantage of our saturation mutagenesis results. We
351 observed that exonic variants with an intact branchpoint-like sequence at positions 10-15
352 (CUAACU) displayed an average inclusion of 45%, whereas variants harbouring mutations
353 at either of the two adenosines that could serve as branch sites in this sequence increased
354 the levels of exon inclusion, and mutation of both adenosines further increased exon
355 inclusion to an average of 75% (**figure 3N**). Also consistent with our model, insertion of AG-
356 containing sequences after position 40 reduced full length exon inclusion, compared to
357 insertion of non-AG-containing sequences, from an average of 75% to 25% inclusion (**figure**
358 **3O**).
359

360 Collectively, our results reveal a novel mechanism of exon skipping based upon assembly of
361 U2 snRNP on exonic sequences that resemble (but cannot be active as) 3' splice sites. This
362 illustrates the value of saturation mutagenesis approaches to discover and test mechanistic
363 hypotheses.

364 **Cryptic 3' splice sites regulate alternative exons encoding one-
365 pass transmembrane helices**

366 It has previously been reported that the Py-tract binding protein U2AF2 binds to an exonic
367 polypyrimidine tract in IL7R exon 6⁴⁷, promoting exon skipping. Like FAS exon 6, IL7R exon
368 6 encodes a one-pass transmembrane helix. Interestingly, transmembrane helices are
369 enriched in nonpolar amino acid residues that are encoded by codons with the highest
370 number of pyrimidines (**figure 4A**). Therefore transmembrane-encoding exons are expected
371 to be rich in pyrimidines, allowing regulation by mechanisms similar to those described for
372 IL7R exon 6 or FAS exon 6 (**figure 3**).

373

374 To investigate whether alternative exons, and particularly those coding for transmembrane
375 domains, are generally regulated by this type of mechanism, we first used SVM-BPfinder⁴⁸ to
376 scan exons throughout the genome harbouring a branchpoint motif followed by a
377 polypyrimidine tract. For each input sequence, this tool returns a score ('SVM score') that
378 reflects how strong a 3' splice site is predicted to be. Interestingly, 23% of all exons had an
379 SVM score greater than that of FAS exon 6 (1.19), suggesting that a significant proportion of
380 exons across the genome may have cryptic 3' splice sites or at least sequence elements that
381 resemble 3' splice site regions. We found that shorter exons (<100 nts) with SVM scores
382 greater than 1.19 encoded the most hydrophobic amino acid sequences (**figure 4B**),
383 consistent with transmembrane domains. These exons had a lower average PSI compared
384 to other exons (**figure 4C**). These results are compatible with the existence of a category of
385 (relatively) short exons containing 3' splice site-like sequences and, in particular, those
386 encoding individual transmembrane helices (**figure 4D**), whose inclusion is decreased by
387 exonic 3' splice site-like sequences.

388

389 To experimentally validate this hypothesis, we built minigenes containing one-pass
390 transmembrane domain-encoding exon 5 of CHODL⁴⁹ and exon 6 of CXADR⁵⁰, and mutated
391 their exonic putative branchpoint adenosines (**figure 4E-F**). In both cases, the mutations
392 reduced exon skipping, suggesting that the levels of exon skipping were regulated by the
393 recognition of 3' splice site-like sequences. Cryptic 3' splice sites in exons may therefore be
394 a widespread mechanism to regulate the inclusion of alternative exons encoding
395 transmembrane helices and thus modulate the balance between soluble and membrane-
396 bound protein isoforms.

397 **Deep learning variant effect predictors accurately predict the
398 effects of different types of genetic variation on alternative
399 splicing**

400 Multiple computational models have been used to predict the effects of genetic variation on
401 splicing. Our deep indel mutagenesis dataset provides a unique opportunity to test the
402 performance of these models for indel mutations, as well as independent evaluation of their
403 accuracy for predicting the effects of substitutions.

404

405 We evaluated the performance of five different models: SMS score (an additive model using
406 7-mer sequences as input features with parameters learnt in a saturation mutagenesis

407 assay⁷), HAL (an additive model using hexamers as input features with parameters learned
408 from millions of random 50-nt-long exonic and intronic sequences⁵¹), MMSplice (a modular
409 neural network where modules were trained to predict the effects of mutations on different
410 splicing-relevant sequence regions⁵²), SpliceAI (a deep learning model trained on human
411 sequencing data⁵³) and Pangolin (a deep learning model based on the SpliceAI architecture
412 but also trained with data from three additional mammalian species⁵⁴).

413
414 All models predicted the effects of single-nt substitutions at least moderately well (**figure**
415 **5A**), with Pangolin showing the best performance ($\rho = 0.82$), followed by SpliceAI ($\rho =$
416 0.79), MMSplice ($\rho = 0.74$), HAL ($\rho = 0.69$) and SMS scores ($\rho = 0.50$). These models
417 had a similar range and order of performance when predicting the effects of all insertions (1-,
418 2-, 3- and 4-nts long) in our library ($\rho = 0.80$ for Pangolin, $\rho = 0.78$ for SpliceAI, $\rho =$
419 0.66 for MMSplice, $\rho = 0.67$ for HAL and $\rho = 0.54$ for SMS scores).

420
421 Interestingly, the predictive performance for deletions was substantially worse for most
422 methods ($\rho = 0.18$ for MMSplice, $\rho = -0.41$ for HAL, and $\rho = 0.17$ for SMS scores)
423 except SpliceAI ($\rho = 0.90$) and Pangolin ($\rho = 0.89$) which remained highly predictive.

424
425 Considering all variants of all types in the library, SpliceAI performed best, with a Spearman
426 correlation of 0.84. Indeed, SpliceAI predictions closely replicated our comprehensive
427 deletion maps (**figure 5B-C**), recapitulating a similar regulatory architecture as that
428 uncovered by our experimental dataset. This opens the possibility that this type of model is
429 used to perform *in silico* deletion mutagenesis experiments and build regulatory maps for
430 other exons as well.

431 *In silico* deletion mutagenesis reveals the regulatory 432 architecture of exons genome-wide

433 To test the utility of *in silico* deletion mutagenesis, we used SpliceAI to predict the effects of
434 all 4 nt deletions in 18,551 exons expressed in at least 80% of GTEx tissues with a length
435 between 50 and 200 nts. The impact of a 4 nt deletion is predicted to depend on each
436 individual exon, although highly-included exons ($PSI > 90\%$) are predicted to be more robust
437 to PSI changes compared to exons included at lower levels (**figure 6A**), an expected
438 consequence of the scaling law that the effects of splicing mutations follow (Baeza et al,
439 2019).

440
441 To systematically analyse the regulatory architecture of exons throughout the genome, we
442 used SpliceAI predictions to train a hidden Markov model with 3 states (**figure 6B**): E
443 (enhancer – corresponding to regions of the exon that promote skipping upon deletion), S
444 (silencer – regions that promote inclusion upon deletion) and N (neutral – which have no
445 consistent effect upon deletion). Our model captured the regulatory architecture of FAS exon
446 6 as uncovered by our deep indel mutagenesis experiment: regions of the exon
447 corresponding to inferred enhancers were predicted to be in state E, and regions
448 corresponding to inferred silencers in state S (**figure 6C**). This suggests that the model can
449 accurately detect splicing regulatory elements along an exon sequence.

450

451 We first used our model to study the distribution of splicing regulatory element (SRE) lengths
452 (i.e. stretches of nts in the same E or S states within an exon) throughout the transcriptome.
453 This revealed that most exonic SREs are short, with a median length of 5 nts and a mean of
454 8.57 nts (compatible with the average binding site of various RNA-binding protein domains^{55–}
455 ⁵⁷) and similar to what we find in FAS exon 6. Enhancers were predicted to be slightly
456 shorter than silencers (median lengths = 4 vs 6 nts; mean lengths = 6.15 vs 10.70 nts; **figure**
457 **6D**). The model also correctly interpreted exonic sequences that are part of splice site
458 sequences and their immediate neighbourhood as inclusion-promoting (i.e. belonging to the
459 E state, **figure 6E**, **figure S13**).

460
461 We next used our model to gain a comprehensive overview of the regulatory architecture of
462 the entire exome. To do this, we used ternary plots to visualise all 18,551 exons in our
463 dataset based on their predicted E/N/S states. This revealed two strong trends. First, for
464 exons shorter than 100 nts, the percentage of nts in the N state tends to be below 20%,
465 irrespective of the proportion of nts in the S or E states, while exons longer than 150 nts tend
466 to have a higher than 20% percentage of nts in the N state (**figure 6F**). This suggests that
467 the inclusion of short exons, such as FAS exon 6, may require a higher density of SREs
468 compared to longer exons. Indeed, as exon length increases, the absolute number of
469 nucleotides in the E or S states rises at a slower rate than expected if the proportion of
470 nucleotides in these states remained constant regardless of exon length (**figure S14**).
471 Second, across highly-included exons, consistently fewer than 20% of nts are in the S state,
472 regardless of the proportion of nts in the N or E states (**figure 6G**). This suggests that
473 maintaining exon inclusion relies more on a low proportion of silencers than on a high
474 proportion of enhancers, as also evidenced by the high inclusion values of exons whose nts
475 predominantly fall into the N state (bottom right-hand corner in **figure 6G**). Interestingly, FAS
476 exon 6, which has intermediate inclusion levels, approximately aligns with this boundary,
477 with 23% of its nts predicted to be in the S state.

478
479 Our deletion analysis revealed not only that nearly the entire sequence of FAS exon 6 is
480 covered by SREs (as is apparently typical of short exons across the genome), but also that
481 its enhancers and silencers alternate in a ‘checkerboard’ pattern along the exon. We used
482 our genome-wide *in silico* deletion mutagenesis to evaluate if this ‘checkerboard’ pattern is
483 likely to be common in additional exons

484
485 We first hypothesised that exons encompassed entirely by SREs arranged in an alternating
486 checkerboard pattern would distribute approximately 50% of their nts in the S state and the
487 remaining 50% in the E state. Our ternary plots suggest that exons meeting this criterion are
488 shorter than 100 nts (**figure 6F**) and display relatively low levels of inclusion (**figure 6G**). We
489 next explicitly evaluated this hypothesis by counting the number of times the sequence of
490 each exon in our dataset transitions from the E to the S state directly, and vice versa –
491 without passing through the N state. For example, in the case of FAS exon 6, we counted 7
492 such transitions (**figure 6C**), equivalent to 9.5 E/S state transitions per 100 nts of exon
493 sequence. The sequences of short (≤ 100 nt long) highly included ($\geq 90\%$) exons were
494 predicted to have very few E/S state transitions, with an average of 1.5 E/S state transitions
495 per 100 nts (**figure S15A**, results for longer exons shown in **figure S14B–C**). In contrast,
496 short alternatively spliced exons included at lower levels ($< 90\%$) had many more state

497 changes (two-tailed Wilcoxon rank sum test p value < 2.2e-16), with an average of 3.7 E/S
498 state transitions per 100 nts (**figure S15A**, results for longer exons shown in **figure S15B-**
499 **C**).

500
501 Repeating this analysis for E/N state transitions (i.e. where the sequence transitions from the
502 E to the N state and vice versa, without passing through the S state) reveals that short
503 highly-included exons have significantly more E/N state transitions per 100 nts compared to
504 short exons with a PSI below 90% (median 2.4 vs 1.4, two-tailed Wilcoxon rank sum test p
505 value < 2.2e-16, **figure S16A**), in agreement with previous findings that constitutive exons
506 are sustained by strong enhancers^{58,59}. Interestingly, this result did not hold true for exons
507 longer than 100 nts (median 1.7 vs 1.8, Wilcoxon rank sum test p value 0.57, **figure S16B-**
508 **C**).

509
510 Alternative exons are therefore predicted to have a high density of splicing regulatory
511 elements, which suggests that their precise inclusion levels are tightly regulated and
512 therefore sensitive to mutation. The alternating pattern of enhancers and silencers further
513 suggests that some of these regulatory domains likely act by modulating the function of a
514 neighbouring domain (e.g. a silencer protein binding to its site might sterically prevent a
515 neighbouring enhancer from being bound by an enhancer protein). On the other hand, the
516 lower density of enhancer-silencer alternations in constitutive exons suggests that their high
517 inclusion levels have not been achieved by fine-tuning binding of splicing regulatory
518 machinery. Their high inclusion levels might therefore simply be a function of their stronger
519 splice sites⁶⁰⁻⁶².

520

521 **Deletion scans accurately predict the effects of antisense 522 oligonucleotides on exon inclusion**

523 Antisense oligonucleotides (AONs) are an increasingly appealing therapeutic strategy to
524 clinically modulate alternative splicing, as recently illustrated by the clinical success of
525 Nusinersen for the treatment of Spinal Muscular Atrophy¹⁶ and Eteplirsen for Duchenne
526 muscular dystrophy¹⁷. AONs base-pair to splice sites or regulatory sequences, competing
527 with the binding of splicing factors and regulators⁶³.

528
529 Clinically-used AONs are typically longer than individual regulatory elements (18-21 nt AONs
530 versus 5-10 nt regulatory motifs), making the prediction of AON effects challenging. We
531 reasoned that deletion mutagenesis might provide a rapid method to predict the effects of
532 AONs binding to different regions of a transcript, since deleting (a set of) regulatory motif(s)
533 will inhibit the assembly of cognate *trans*-acting regulatory factors, which is also the
534 mechanism of action of AONs, as they typically compete with the binding of *trans*-acting
535 factors to the same sequences (**figure 7A**).

536

537 We compared the effects on splicing of an array of partially overlapping AONs collectively
538 covering the entire length of FAS exon 6 (AON walk) with the effects of deletions of the
539 same length (deletion walk). Changes in exon inclusion correlated well for 21-nt AONs and
540 21-nt deletions spaced every 5nt along the exon (Spearman rho = 0.75, n=9, **figure 7B**).
541 These AONs modulate exon 6 inclusion over a wide dynamic range (from 20% to 50%

542 inclusion, compared with the approximately 50% inclusion level of the WT exon). The
543 correlation between the AON effects and the SpliceAI-predicted effects of 21-nt deletions
544 was similarly strong ($\rho = 0.74$, **figure 7C**), suggesting that *in silico* deletion mutagenesis
545 could be an efficient, affordable strategy to identify regions in an exon that can be targeted
546 by AONs to achieve a range of desired splicing outcomes for therapeutic or biotechnological
547 applications.

548 DANGO: a genome-wide resource for AON discovery

549 We used SpliceAI to predict the effects of all possible 21-nt deletions across the exome to
550 generate a resource we refer to as DANGO (Deletion/ANtisense oliGO – with each DANGO
551 score corresponding to the SpliceAI predictions for a particular 21-nt deletion). 12.4% of all
552 21nt deletions had an absolute DANGO score greater than 0.1 (mean absolute DANGO
553 score across the exome = 0.05). Short exons (≤ 100 nt) were most vulnerable to these
554 deletions (**figure 7D**), with 44.8% of all 21nt deletions in these exons having an absolute
555 DANGO score > 0.1 , compared to 10.2% in longer exons. Varying the DANGO score
556 threshold (0.025, 0.05, 0.2, or 0.4) altered the proportion of deletions considered impactful,
557 but it did not change the fundamental finding that short exons are more sensitive to the
558 effects of 21nt deletions.

559
560 Regardless of the length of the exon, the proportion of negative DANGO scores is greater
561 than the proportion of positive scores (**figure 7E**). This suggests that AONs targeting exonic
562 regions are more likely to reduce recognition of the exon, rather than increase inclusion.

563
564 To visualise our results on an exon-by-exon basis, we generated a custom genome browser
565 track (**supplementary data 1**) displaying the DANGO scores for all exons in the genome.
566 This track allows users to interactively explore exonic regions of interest for sequences that
567 may be susceptible to splicing changes upon 21-nt deletions. Visualising FAS exon 6 reveals
568 that DANGO scores cluster around the identified regulatory domains of this exon (**figure 7F**),
569 suggesting that these scores can accurately reflect the regulatory architecture of exonic
570 sequences. Interestingly, since 21-nt deletions push FAS exon 6 below the length threshold
571 for exon definition (**figure 3A**), nearly all 21mer deletions in this exon are predicted to
572 promote skipping (**figure 7F**) and do, in, fact, promote skipping as demonstrated in our
573 experimental assay (**figure 5B**), but deletions spanning silencer regions promote less
574 skipping than deletions spanning enhancer regions.

575
576 DANGO is therefore a genome-wide resource that accurately predicts the effects of 21-nt
577 deletions that can be used for AON selection.

578

579 Discussion

580 Here, by comprehensively quantifying the effects of substitutions, insertions and deletions on
581 splicing we have shown that experimental and *in silico* deletion scanning are particularly
582 effective strategies for revealing the splicing regulatory landscape of exons and we have

583 provided a first overview of the exonic splicing regulatory landscape of the human genome.
584 Moreover, we have shown that deletion scanning accurately predicts the effects of AONs on
585 exon inclusion and have provided a resource, DANGO, to facilitate AON design genome-
586 wide. Finally, by analysing the effects of insertions, we have discovered a novel regulatory
587 mechanism whereby the inclusion of short exons encoding one-pass transmembrane
588 domains is repressed by the binding of a core component of the spliceosome that normally
589 recognizes introns, U2 snRNP, to exons. This recognition of cryptic intron-like sequences in
590 exons provides a simple mechanism for the evolutionary birth of short microexons.

591

592 The FAS exon 6 regulatory landscape has a checkerboard organisation of alternating
593 silencers and enhancers that cover the entire exon. *In silico* deletion scans indicate that this
594 architecture is not unusual, but typical of short alternatively spliced exons. The dense
595 splicing regulatory landscape of human exons (Figure 6) is remarkable and a valuable
596 resource to be further explored in future work.

597

598 Collectively, our results highlight the power of deep indel mutagenesis for charting regulatory
599 landscapes, generating novel mechanistic hypotheses, and deriving biological insights. One
600 shortcoming of our study is that we have only considered exonic sequences. In future work it
601 will be important to extend deletion scanning to introns and to quantify the effects of
602 inhibiting combinations of intronic and exonic regulatory sequences, potentially allowing finer
603 control of desired splicing changes using AONs. Indeed, we envisage that both *in silico* and
604 high-throughput experimental deletion scans will play an increasingly important role in
605 accelerating the discovery of AONs to effectively modulate splicing for many different
606 therapeutic goals.

607

608

609

610

611

612

613

614 Methods

615 Indel library construction

616 A sequence library was designed to include: 63-nt-long wild-type sequence of FAS exon 6,
617 all possible 189 single-nt substitutions, all 2010 possible deletions ranging in length from 1 to
618 60 nts, all 5208 possible 1-, 2-, and 3-nt-long insertions as well as 400 randomly-selected 4-
619 nt insertions (full library design along with measured PSI values available in **Supplementary**
620 **Table 1**). The library was synthesised and purified by Twist Bioscience.
621

622 Indel library amplification

623 Oligo libraries were resuspended in 10 mM Tris buffer, pH 8.0 to a concentration of 20 ng/ul.
624 20 ng of template ssDNA Twist library were PCR amplified with Pfx Accuprime polymerase
625 (Thermo scientific, 12344024) in a total reaction volume of 50 ul in quadruplicate, for 12
626 cycles (as recommended by Twist Bioscience for a 100-150 nt oligo pool) using the following
627 flanking intronic primers: FAS_i5_GC_F (5'-tgtccaatgttccaacctacag-3') and FAS_i6_GC_R
628 (5'-ctacttccaagttattcaatctg-3'). PCR reactions were combined and cleaned-up with the
629 Quiaquick PCR purification kit, eluted with 50 ul elution buffer and dsDNA measured with a
630 NanoDrop spectrophotometer.
631

632 Indel library subcloning

633 The amplified library was recombined with pCMV FAS wt minigene exon 5-6-7⁴⁶. We used a
634 vector:insert ratio of 1:8, using 150 ng of vector backbone and 20 ng of dsDNA amplified
635 libraries and incubated at 50°C for two hours for DNA assembly, using a Gibson master mix
636 developed at the CRG Protein Technologies Unit, which contains a mix of T5 exonuclease
637 (T5E4111K 1000U from Epicentre Biotech-Ecogen), Phusion polymerase (F530s 100U from
638 VITRO and a Taq DNA ligase (Protein Technologies Unit CRG, homemade). After
639 transformation into Stellar competent cells (Clontech, 636766), combining five replicates in
640 order to maximise the number of individual transformants amplified, cells were grown for 18
641 hours in LB medium containing ampicillin. We obtained approximately 4.29 million clones.
642 After bacterial transformation, the final plasmid library was purified using the Qiagen
643 plasmid maxi kit (50912163, Quiagen) and quantified with a NanoDrop spectrophotometer.
644

645 Transfection of Hek293 cell line to generate output libraries

646 750,000 Hek293 cells were plated on 100x20 mm petri dishes and transfected with 80 ng
647 cloned libraries in 8 ml OPTIMEM Reduced Serum Medium with no phenol Red (Life
648 technologies, 11058021) using Lipofectamine 2000 (Life technologies, 11668019) in nine
649 biological replicates. 48h post transfection, cells were collected and RNA was prepared
650 using Maxwell simplyRNA Tissue Kit (Promega, AS1280). cDNA was prepared with 400 ng
651 total RNA using specific vector backbone PT2 primer (5'- AAGCTTGCATCGAATCAGTAG -

652 3') and Superscript III reverse transcriptase (Thermo Fisher, 18080085). PCR amplification
653 of cDNA samples was performed with GoTaq flexi (PROMEGA, M7806) using a distinct 8-
654 mer barcoded oligos to distinguish the nine experimental replicates. PCR products were run
655 on a 2% agarose gel and the smear corresponding to sizes of the amplification product
656 expected from exon inclusion (full length and insertion and deletion mutants) was excised,
657 purified using the Quiaquick Gel extraction kit (Qiagen, 50928704) and quantified with a
658 NanoDrop spectrophotometer.
659

660 Input indel library

661 20 ng of the plasmid library were amplified in triplicates using GoTaq flexi DNA polymerase
662 (M7806, Promega) for 25 cycles with three different pairs of barcoded intronic primers
663 FAS_i5_TR_F and PT2 (“Indel library amplification primers” in **Supplementary Table 2**).
664 Since the insertions and deletions result in a library with exons of different length, this
665 resulted in a PCR smear (corresponding to exons ranging in length from 3 to 67 nts), which
666 was gel-purified and sequenced. Each pair of primers had a distinct 8-mer barcode
667 sequence to discriminate between technical replicates (“Primers used for amplifying
668 technical replicates (input library)” in **Supplementary Table 2**).
669
670

671 Sequencing

672 Equimolar quantities of three independent amplifications of the input library and equimolar
673 quantities of the purified inclusion smear (output library) of each of the nine replicates were
674 pooled and sequenced at the CRG Genomics Core Facility where Illumina Ampliseq PCR-
675 free libraries were prepared and run on a single lane of an Illumina HiSeq2500. In total, 424
676 million paired-end reads were obtained (188 and 236 million for input and output
677 respectively). The median sequencing coverage for all exon variants in the input was 2114
678 reads. In the output, the median sequencing coverage was between 278 and 468 reads.
679 Raw sequencing data has been submitted to GEO with accession number GSE244179.
680

681 Data processing and calculation of PSI values

682 FastQ files from paired-end sequencing were processed with DiMSum v1.2.7⁶⁴ using default
683 settings with minor adjustments (<https://github.com/lehner-lab/DiMSum>). First, DiMSum was
684 run in default paired-end mode to demultiplex reads into input and replicate output samples
685 (Stage 0 only). Second, DiMSum Stages 1-5 were run in single-end mode ('--paired' = F)
686 using only demultiplexed forward reads that have full coverage of the exon sequence.
687 Reverse reads, originally intended to cover a unique molecular identifier (UMI) and a 3'
688 portion of the exon sequence, were discarded. The final stage estimates an enrichment
689 score (ES) and associated error for each mutant variant based on its frequency in the input
690 and output libraries, and relative to the wild type sequence in both libraries. Experimental
691 design files and command-line options required for running DiMSum on this dataset are
692 available on GitHub (<https://github.com/lehner-lab/fas-indel-library>).

693

694

695 The PSI of the wild type FAS exon 6 sequence has been previously experimentally shown to
696 be 49.1%⁵. Therefore, the PSI of a variant of interest is estimated as follows:

697

698
$$\frac{PSI_{variant}}{PSI_{WT}} = \frac{ES_{variant}}{ES_{WT}}$$

699

700
$$PSI_{variant} = PSI_{WT} \cdot \frac{ES_{variant}}{ES_{WT}}$$

701

702
$$PSI_{variant} = 49.1 \cdot \frac{ES_{variant}}{ES_{WT}}$$

703

704

705 Experimental validation of estimated PSI values

706

707 To confirm the accuracy of our PSI estimates on single-nt substitutions, we took the
708 previously experimentally-determined values of 25 exon variants⁵ and plotted them against
709 the experimentally-determined values (Figure 1C). To validate our estimates of indel PSI
710 values, 15 individual clones from the indel library were Sanger sequenced. They covered a
711 wide range of estimated PSI and were therefore good for validation and checking correlation.

712

713 Individual mutants were transfected into Hek293 cells in triplicates to quantify the ratio
714 between exon 6 inclusion and skipping. For RT-PCR, minigene-specific primers were used
715 ("Primers used for amplifying biological replicates (Output library)" in **Supplementary Table**
716 **2**). To avoid amplification of endogenous FAS RNAs, these primers (PT1 and PT2) are
717 complementary to a plasmid backbone sequence distinct from endogenous DNA. RT-PCR
718 products were fractionated by electrophoresis using 6% polyacrylamide gels in 1 x TBE and
719 Sybr safe staining (ThermoFisher Scientific, S33102). The bands corresponding to exon
720 inclusion or skipping were quantified using ImageJ v1.47 (NIH, USA). PSI measurements
721 are shown in **Supplementary Table 3**.

722

723 Under the particular experimental conditions in which these indel mutants were tested, the
724 wild-type exon was included with a PSI of 49.9% (compared to 49.1% in the experiment
725 done to validate the single nt substitutions⁵). To visualise these results in the same plot as
726 the single-nt substitutions (Figure 1C), we used the splicing scaling law⁶⁵ to adjust all
727 experimentally-determined PSI values to what their values should have been if the wild type
728 had a PSI of 49.1%.

729

730 Estimating PSI values in the GTEx dataset

731 We estimated the PSI of exons in the GTEx dataset (GTEx Consortium, 2017) from the
732 proportion of reads supporting exon inclusion in the GTEx junction read counts file

733 **(GTEx_Analysis_2016-01-15_v7_STARv2.4.2a_junctions.gct.gz**; available for download
734 at <https://www.gtexportal.org/home/datasets>). To do this, we used the *quantifySplicing*
735 function from the Psichomics package in R⁶⁶. The *minReads* argument was set to 10 (such
736 that a splicing event requires at least 10 reads for it to be quantified) and the *eventType*
737 argument was set to 'SE' (instructing the *quantifySplicing* function to quantify alternative
738 exon events). All estimates were based on the Psichomics hg19/GRCh37 alternative splicing
739 annotations.

740
741

742 Experimentally validating microexon inclusion

743 We initially cloned the microexon sequences observed in the output (i.e. those sequences
744 corresponding to large deletions, **figure S11A**) into our plasmid vector backbone
745 (pCMV_FAS_exon4_exon6) and transfected them. No inclusion band was found in the
746 polyacrylamide gels (i.e. these sequences were 100% skipped, **figure S11B**).

747 Since the nt composition of the PTB binding domain in the central region of FAS exon 6 is
748 very similar to the polypyrimidine tract of a 3' splice site, we reasoned that an AG-containing
749 insertion right after nt 40 (e.g. CAG, AG, TA, A, CTA) could create a new 3' splice site in this
750 region of the exon. Such a splice site would produce the microexons detected in the deep
751 mutagenesis experiment. We introduced these insertions (as well as the non-AG-containing
752 GAC insertion as a negative control) into the vector backbone using site-directed
753 mutagenesis (Agilent, 200523) using the relevant mutagenesis primers. These minigene
754 constructs were transfected into Hek293 cells in triplicate. RT-PCR products were
755 fractionated by electrophoresis on 6% native acrylamide gels.

756
757
758

759 Experimentally testing exon inclusion with different splice sites

760 To test the effects of mutations in the presence of different 3' splice site strengths, we used
761 partially complementary oligonucleotides in combination with TaqPlus precision
762 (Agilent, 600212) and PCR "around the world" (primers pointing in opposite directions from
763 the mutagenesis site to amplify the full length of the plasmid) to replace the naturally weak 3'
764 splice site of FAS exon 6 (UUUCAUAUAAAUGUCCAAUGUUCCAACCUACAG) with a
765 strong 3' splice site sequence (UACUAACGGCUUUUUUUCCUUUUUCAG).

766

767 PTB/SRRM4 overexpression experiments

768 We overexpressed the SRRM4 (or PTBP1) protein by co-transfected minigenes containing
769 a CAG or AG insertion after position 40 along with 1000 ng of pcDNA5_SRRM4_flag (or
770 pcDNA5_PTBP1_T7) in lipofectamine 2000 for 24 hours. RT-PCR was then used to analyse
771 the splicing ratios as described above.

772
773

774 In vitro transcription experiments

775 T7 promoter-containing transcription templates were generated by PCR using Gotaq flexi
776 enzyme (Promega, M7806): FAS exon 6 WT/noBP templates were generated from FAS WT
777 minigene, Fas M0 template was generated from Fas M0 minigene (Izquierdo et al, 2007),
778 FAS exon 6 UAG mutant template was generated from a ssDNA oligonucleotide. PCR
779 products were purified on agarose gel.

780

781 Cy5-CTP/Cy5-UTP labelled RNA were transcribed directly from the PCR templates using
782 Megascript T7 Transcription kit (Ambion) according to the manufacturer's instructions. A
783 complex formation 15 ng/ul fluorescently labelled RNA were incubated with 3 ul of HeLa cell
784 nuclear extracts (CILBIOTECH, CC-01-20-50) supplemented with 3 mM MgCl₂, 24.9 mM
785 KCl, 3.33% PVA, 13.3 mM HEPES pH 8, 0.13 mM EDTA, 13.3 % glycerol, 0.03 % NP-40,
786 0.66 mM DTT, 2 mM ATP and 22 mM creatine phosphate in a final volume of 9 ul. The
787 mixture was incubated for 18 min at 30°C. 1 microliter of heparin (10 ug/ul stock) was added
788 and incubated for 10 min at room temperature. 3 ul of 50% glycerol were added and 9 ul
789 loaded on a composite gel (4% acrylamide, 0.05% bis-acrylamide, 0.5% agarose, 50mM
790 Tris, 50mM glycine).

791

792 The gel was run for 6 hours at 200 Volts in 50mM Tris / 50mM glycine buffer. After
793 electrophoresis, fluorescence was detected using a Typhoon PhosphorImager. The
794 inactivation of U1 snRNP and U2 snRNP was performed as described in Dönmez et al⁶⁷
795 using 2'-O-methylated oligoribonucleotide complementary to U1 snRNA (5'-
796 CUGCCAGGUAAGUAU-3') or U2 snRNA (5'-CAGAUACUACACUUG-3').

797

798

799 Scanning the exome for sequences similar to 3' splice sites

800 To identify exonic sequences similar to 3' splice sites in our GTEx dataset (see **Estimating**
801 **PSI values in the GTEx dataset** section), we used SVM-BPfinder, a support vector
802 machine that scores how closely a nt sequence resembles a 3' splice site preceded by a
803 branchpoint⁴⁸. SVM-BPfinder was run at each position of each exon with the *--species*
804 argument set to Hsap, the *--max-len* argument set to 1000, and the *--min-dist* argument set
805 to 15. The final score assigned to each exon was the maximum score across all of its
806 positions. This corresponds to the sequence within the exon that most closely resembles a 3'
807 splice site.

808

809 Measuring hydropathy in exons throughout the genome

810 To measure hydropathy, the *hydrophobicity* function from the *Peptides* package⁶⁸ in R was
811 used with the *scale* argument set to "KyleDoolittle".

812

813 **Preparation of minigene constructs carrying a transmembrane
814 domain (CHODL exon 5 and CXADR exon 6)**

815 Genomic DNA sequences were amplified from commercial genomic DNA (PROMEGA,
816 G304A), and branch site mutations were produced with the help of Taq Plus precision
817 (Agilent, 600212). Sequences of genomic regions were cloned into the pCMV_FAS567
818 minigene replacing FAS exon 6. The amplified genomic sequences were:

819 **CHODL exon 5 (103 bp) GRCh37/hg19 chr21:19635108-19635210**

820 GTATAATTCCCAATCTAATTATGTTGTTACCAACAATACCCCTGCTCTACTGATACT
821 GGTTGCTTTGGAACCTGTTGTTCCAGATGCTGCATAAAAG

822 **CXADR exon 6 (139 bp) GRCh37/hg19 chr21:18933656-18933794**

823 CTTCAAATAAAGCTGGACTAATTGCAGGAGCCATTATAGGAACCTTGCTGCTCTAGCG
824 CTCATTGGTCTTATCATCTTGCTGTCGAAAAAGCGCAGAGAAGAAAAATATGAAAAG
825 GAAGTTCATCACGATATCAG

826 Minigene constructs with the wild type exons contained the amplified genomic sequences
827 above. In the case of exons whose putative branchpoint adenines were mutated and
828 substituted with guanines, the minigene constructs contained the following exonic
829 sequences:

830 **CHODL exon 5**

831 GTATAATTCCCAATCTAATTATGTTGTTACCAACAATACCCCTGCTCTGCTGGTGC
832 TGGTTGCTTTGGAACCTGTTGTTCCAGATGCTGCATAAAAG

833 **CXADR exon 6**

834 CTTCAAATAAAGCTGGACTAATTGCAGGAGCCATTATAGGAACCTTGCTGCTCTAGCG
835 CTCGTTGGTCTTCTCGTCTTGCTGTCGAAAAAGCGCAGAGAAGAAAAATATGAAAAG
836 GGAAGTTCATCACGATATCAG

837 Sequences were all confirmed by Sanger sequencing of acrylamide purified PCR bands by
838 crush and soak method. All minigene constructs were confirmed by Sanger sequencing.
839

840 **Predicting FAS exon 6 mutation effects using SMS Scores**

841 We downloaded Supplementary Table 7 from Ke et al.⁷, which lists the SMS scores for all
842 possible 7-mers. To calculate the total SMS score for each exon in our indel library, we
843 performed a sliding window analysis by adding the SMS scores of consecutive 7-mers along
844 its sequence. The final SMS score for each variant was obtained by subtracting the total
845 SMS score for the wild type exon from that of the variant:

846

847
$$SMS_{final(variant)} = SMS_{total(variant)} - SMS_{total(wild\ type)}$$

848

849 Predicting FAS exon 6 mutation effects using HAL

850 To predict the effects of exon variants on inclusion with HAL⁵¹, we uploaded a file containing
851 the sequences in our library to <http://splicing.cs.washington.edu/SE> using 49.1% as the wild
852 type levels of inclusion. An output file was returned that contains the predicted PSI values for
853 each sequence in the input file.

854

855 Predicting FAS exon 6 mutation effects using MMSplice

856 We converted our indel library design file to VCF format, and used this new file as input for
857 MMSplice⁵². We ran the algorithm online, on the Google Colab notebook provided for this
858 purpose (available at
859 <https://colab.research.google.com/drive/1Kw5rHMXaxXXsmE3WecxbXyGQJma80Eq6>).
860 This returned a CSV file with multiple columns containing different metrics for each exon
861 variant. We selected *delta_logit_psi* as the predictor for the mutation effects.
862

863 Predicting FAS exon 6 mutation effects using SpliceAI

864 We converted our indel library design file to VCF format, and used this new file as input for
865 SpliceAI⁵³. We ran SpliceAI using GRCh38 as both the genome reference and gene
866 annotation files. All other parameters were set to the default configuration (parameter “D”,
867 the maximum distance between the variant and gained/lost splice site was left to its default
868 of 50, which means that the algorithm could be capturing information about splice site gain
869 and loss beyond the boundaries of the exon). As SpliceAI outputs four scores for each
870 mutant sequence (corresponding to splice site acceptor loss, splice site acceptor gain, splice
871 site donor loss, and splice site donor gain), we selected the score associated with the
872 highest absolute value in each case. If this score corresponded to a splice site loss, the
873 score was multiplied by minus 1.

874 Predicting FAS exon 6 mutation effects using Pangolin

875 We converted our indel library design file to VCF format, and used this new file as input for
876 the Google Colab Notebook made available by the authors of Pangolin⁵⁴ at
877 <https://colab.research.google.com/github/tkzeng/Pangolin/blob/main/PangolinColab.ipynb>.
878 Pangolin was used with the default options chosen for the Colab Notebook, including
879 GRCh37 as the genome reference. Like SpliceAI, Pangolin outputs four scores for each
880 mutant sequence (corresponding to splice site acceptor loss, splice site acceptor gain, splice
881 site donor loss, and splice site donor gain). The Pangolin score selected for each mutation
882 corresponded to that with the highest absolute value out of these four. If this score
883 corresponded to a splice site loss, the score was multiplied by minus 1.
884

885 *In silico* 4mer deletions in exons genome-wide

886 The SpliceAI developers created a file with annotations for all possible substitutions, 1 base
887 insertions, and 1-4 base deletions across the genome. This file is available for download at
888 <https://basespace.illumina.com/s/otSPW8hnhZR>. We downloaded the file and extracted
889 4mer deletion data for all exons we calculated PSI values for (see **Estimating PSI values in**
890 **the GTEx dataset** section). For each 4mer deletion in these exons, we computed its
891 SpliceAI score by taking the maximum value among the acceptor gain, acceptor loss, donor
892 gain, and donor loss scores. If the maximum value was the acceptor loss or the donor loss
893 score, we multiplied the value by -1.
894

895 Hidden Markov model

896 We used the *depmixS4* package in R to build a hidden Markov model that predicts the
897 locations of exonic splicing enhancers (which promote exon inclusion) and silencers (which
898 promote skipping) in each exon based on SpliceAI scores for 4mer deletions (see section
899 above titled ***in silico* 4mer deletions in exons genome-wide**). Exons with lengths between
900 50 and 200 nts were used as input for the model, with each exon as a separate time series
901 during training. The model has three hidden states: E (enhancer), N (neutral), and S
902 (silencer), with mean scores of -0.15, 0, and 0.15, respectively. The standard deviations for
903 the states were fixed at 0.1, 0.025, and 0.1 to account for the variability of positive and
904 negative values in the dataset. For example, although breaking a splice site has a much
905 stronger effect than breaking a weak enhancer (resulting in a much more negative spliceAI
906 score), both sequence elements should be classified together in the E state.
907

908 AON Walk

909 100,000 HEK293 cells in a 6-well plate were transfected with Antisense oligonucleotide
910 harbouring 2'-O Me phosphorothioate modifications at each nucleotide position (Integrated
911 technologies) using 3 ul of Lipofectamine 2000 (11668027, ThermoFisher Scientific) in one
912 ml OPTIMEM I Reduced Serum Medium with no phenol red (11058021, ThermoFisher
913 Scientific) to a final concentration of 2.5 nMolar (exact sequences shown in **Supplementary**
914 **Table 4**). Six hours post-transfection, the cell culture medium was replaced with DMEM
915 Glutamax (61965059, ThermoFisher Scientific) containing 10% FBS and Pen/Strep
916 antibiotics. 24 hours post-transfection, total RNA was isolated using the automated Maxwell
917 LEV 16 simplyRNA tissue kit (AS1280, Promega). cDNA was synthesised with 400 ng total
918 RNA using Superscript III (18080085, Life Technologies) with a mix of random primers and
919 oligodT. Effects on endogenous FAS exon 6 inclusion were determined by PCR using
920 GoTaq flexi DNA polymerase (M7806, Promega) and the following primers:
921 FAS_e5_for 5'-TGTGAAACATGGAATCATCAAGG-3'
922 FAS_e7_endo_R 5'-AAAGTTGGAGATTGATGAGAAC-3'
923

924 Exome-wide 21mer deletion scan

925 After validating the ability of SpliceAI to predict AON effects, we characterised the AON
926 targetability across the genome by performing an exon-wide scan of deletions using SpliceAI
927 scores as a proxy for targetability. Specifically, for all exons in the genome, we produced
928 SpliceAI scores for each length-21 deletion within each of the exons' boundaries. To compile
929 the list and sequences of each exon, we used R package *biomaRt*⁶⁹ with the
930 *hsapiens_gene_ensembl* dataset. We limited the analyses to canonical exons only (referring
931 to the *transcript_is_canonical* attribute of each exon). After compiling the list of all exons and
932 each of their length-21 deletions, we passed each sequence to SpliceAI using the
933 parameters as described under **Predicting FAS exon 6 mutation effects using SpliceAI**.
934 The resulting scores are referred to as the “DANGO scores” of each exon.
935

936 Statistical tests

937 All statistical tests were performed in R 3.6.2 using custom code (see **Code availability**
938 section).
939
940

941 Code availability

942 All scripts used in this study have been made available at the following GitHub repository:
943 <https://github.com/lehner-lab/fas-indel-library>.
944
945
946

947 Data availability

948 DNA sequencing data have been deposited in the Gene Expression Omnibus under the
949 accession number GSE244179.
950

951 Availability of biological materials

952 All deep mutagenesis libraries used in this study are available upon request.
953
954

955 Author contributions

956 PB-C, AJF, MT and GQ performed computational analyses; BM and SB performed
957 experiments; PB-C, BL and JV wrote the manuscript with input from all authors.
958
959

960

961 **Acknowledgements**

962 The authors would like to thank Manuel Irimia for insightful comments and discussion. This
963 work was funded by European Research Council (ERC) Advanced (670146I, 883742)
964 grants, the Spanish Ministry of Science and Innovation (PID2020-114630GB-I00,
965 LCF/PR/HR21/52410004, EMBL Partnership, Severo Ochoa Centre of Excellence), the
966 Bettencourt Schueller Foundation, the AXA Research Fund, Agencia de Gestio d'Ajuts
967 Universitaris i de Recerca (AGAUR, 2017 SGR 1322), and the CERCA Program/Generalitat
968 de Catalunya. GQ was supported by PRE2022-102744, financed by
969 MCIN/AEI/10.13039/501100011033 and FSE+. The Genotype-Tissue Expression (GTEx)
970 data used for the analyses described in this manuscript were obtained from the GTEx Portal
971 on May 8, 2018 and dbGaP accession number phs000424.v7.p2 on May 8, 2018. The GTEx
972 Project was supported by the Common Fund of the Office of the Director of the NIH and by
973 NCI, NHGRI, NHLBI, NIDA, NIMH, and NINDS.
974

975 **Competing Interests**

976 CRG has filed a patent (European Priority Application 24382126.0) for the use of deep indel
977 mutagenesis as a method to identify and predict the effects of antisense oligonucleotides.
978 PB-C, BM, BL and JV are listed as co-inventors. JV is a member of the Scientific Advisory
979 Boards of Remix Therapeutics, Stoke Therapeutics and IntronX. The other authors declare
980 no competing interests.
981
982
983
984

985 References

986

987 1. Braunschweig, U., Guerousov, S., Plocik, A. M., Graveley, B. R. & Blencowe, B. J.
988 Dynamic integration of splicing within gene regulatory pathways. *Cell* **152**, 1252–1269
989 (2013).

990 2. Anna, A. & Monika, G. Splicing mutations in human genetic disorders: examples,
991 detection, and confirmation. *J. Appl. Genet.* **59**, 253–268 (2018).

992 3. Scotti, M. M. & Swanson, M. S. RNA mis-splicing in disease. *Nat. Rev. Genet.* **17**, 19–
993 32 (2016).

994 4. Sterne-Weiler, T. & Sanford, J. R. Exon identity crisis: disease-causing mutations that
995 disrupt the splicing code. *Genome Biol.* **15**, 201 (2014).

996 5. Julien, P., Miñana, B., Baeza-Centurion, P., Valcárcel, J. & Lehner, B. The complete
997 local genotype-phenotype landscape for the alternative splicing of a human exon. *Nat.*
998 *Commun.* **7**, 11558 (2016).

999 6. Braun, S. *et al.* Decoding a cancer-relevant splicing decision in the RON proto-
1000 oncogene using high-throughput mutagenesis. *Nat. Commun.* **9**, 1–18 (2018).

1001 7. Ke, S. *et al.* Saturation mutagenesis reveals manifold determinants of exon definition.
1002 *Genome Res.* **28**, 11–24 (2018).

1003 8. Baeza-Centurion, P., Miñana, B., Valcárcel, J. & Lehner, B. Mutations primarily alter the
1004 inclusion of alternatively spliced exons. *Elife* **9**, (2020).

1005 9. Soemedi, R. *et al.* Pathogenic variants that alter protein code often disrupt splicing. *Nat.*
1006 *Genet.* **49**, 848–855 (2017).

1007 10. Cheung, R. *et al.* A Multiplexed Assay for Exon Recognition Reveals that an
1008 Unappreciated Fraction of Rare Genetic Variants Cause Large-Effect Splicing
1009 Disruptions. *Mol. Cell* **73**, 183–194.e8 (2019).

1010 11. Montgomery, S. B. *et al.* The origin, evolution, and functional impact of short insertion-
1011 deletion variants identified in 179 human genomes. *Genome Res.* **23**, 749–761 (2013).

1012 12. Mullaney, J. M., Mills, R. E., Pittard, W. S. & Devine, S. E. Small insertions and
1013 deletions (INDELs) in human genomes. *Hum. Mol. Genet.* **19**, R131–6 (2010).

1014 13. Stenson, P. D. *et al.* The Human Gene Mutation Database: building a comprehensive
1015 mutation repository for clinical and molecular genetics, diagnostic testing and
1016 personalized genomic medicine. *Hum. Genet.* **133**, 1–9 (2014).

1017 14. Zhang, X. *et al.* Impact of human pathogenic micro-insertions and micro-deletions on
1018 post-transcriptional regulation. *Hum. Mol. Genet.* **23**, 3024–3034 (2014).

1019 15. Rogalska, M. E., Vivori, C. & Valcárcel, J. Regulation of pre-mRNA splicing: roles in
1020 physiology and disease, and therapeutic prospects. *Nat. Rev. Genet.* **24**, 251–269
1021 (2023).

1022 16. Qiu, J. *et al.* History of development of the life-saving drug ‘Nusinersen’ in spinal
1023 muscular atrophy. *Front. Cell. Neurosci.* **16**, 942976 (2022).

1024 17. Sheikh, O. & Yokota, T. Pharmacology and toxicology of eteplirsen and SRP-5051 for
1025 DMD exon 51 skipping: an update. *Arch. Toxicol.* **96**, 1–9 (2022).

1026 18. Kim, J. *et al.* A framework for individualized splice-switching oligonucleotide therapy.
1027 *Nature* **619**, 828–836 (2023).

1028 19. Popplewell, L. J., Trollet, C., Dickson, G. & Graham, I. R. Design of phosphorodiamidate
1029 morpholino oligomers (PMOs) for the induction of exon skipping of the human DMD
1030 gene. *Mol. Ther.* **17**, 554–561 (2009).

1031 20. Harding, P. L., Fall, A. M., Honeyman, K., Fletcher, S. & Wilton, S. D. The influence of
1032 antisense oligonucleotide length on dystrophin exon skipping. *Mol. Ther.* **15**, 157–166
1033 (2007).

1034 21. Pramono, Z. A. D. *et al.* A prospective study in the rational design of efficient antisense
1035 oligonucleotides for exon skipping in the DMD gene. *Hum. Gene Ther.* **23**, 781–790
1036 (2012).

1037 22. Wee, K. B. *et al.* Dynamics of co-transcriptional pre-mRNA folding influences the
1038 induction of dystrophin exon skipping by antisense oligonucleotides. *PLoS One* **3**,
1039 e1844 (2008).

1040 23. Aartsma-Rus, A., Houlleberghs, H., van Deutekom, J. C. T., van Ommen, G.-J. B. & 't
1041 Hoen, P. A. C. Exonic sequences provide better targets for antisense oligonucleotides
1042 than splice site sequences in the modulation of Duchenne muscular dystrophy splicing.
1043 *Oligonucleotides* **20**, 69–77 (2010).

1044 24. Papoff, G. *et al.* An N-terminal domain shared by Fas/Apo-1 (CD95) soluble variants
1045 prevents cell death in vitro. *J. Immunol.* **156**, 4622–4630 (1996).

1046 25. Liu, C., Cheng, J. & Mountz, J. D. Differential expression of human Fas mRNA species
1047 upon peripheral blood mononuclear cell activation. *Biochem. J* **310** (Pt 3), 957–963
1048 (1995).

1049 26. Cheng, J. *et al.* Protection from Fas-mediated apoptosis by a soluble form of the Fas
1050 molecule. *Science* **263**, 1759–1762 (1994).

1051 27. Cascino, I., Fiucci, G., Papoff, G. & Ruberti, G. Three functional soluble forms of the
1052 human apoptosis-inducing Fas molecule are produced by alternative splicing. *J.*
1053 *Immunol.* **154**, 2706–2713 (1995).

1054 28. Agrebi, N. *et al.* Rare splicing defects of FAS underly severe recessive autoimmune
1055 lymphoproliferative syndrome. *Clin. Immunol.* **183**, 17–23 (2017).

1056 29. Ustianenko, D., Weyn-Vanhentenryck, S. M. & Zhang, C. Microexons: discovery,
1057 regulation, and function. *Wiley Interdiscip. Rev. RNA* **8**, (2017).

1058 30. Liu, H. X., Zhang, M. & Krainer, A. R. Identification of functional exonic splicing
1059 enhancer motifs recognized by individual SR proteins. *Genes Dev.* **12**, 1998–2012
1060 (1998).

1061 31. Jain, N., Lin, H.-C., Morgan, C. E., Harris, M. E. & Tolbert, B. S. Rules of RNA specificity
1062 of hnRNP A1 revealed by global and quantitative analysis of its affinity distribution. *Proc.*
1063 *Natl. Acad. Sci. U. S. A.* **114**, 2206–2211 (2017).

1064 32. Yu, Y. *et al.* Dynamic regulation of alternative splicing by silencers that modulate 5'
1065 splice site competition. *Cell* **135**, 1224–1236 (2008).

1066 33. Vo, T. *et al.* HNRNPH1 destabilizes the G-quadruplex structures formed by G-rich RNA
1067 sequences that regulate the alternative splicing of an oncogenic fusion transcript.
1068 *Nucleic Acids Res.* **50**, 6474–6496 (2022).

1069 34. Paronetto, M. P. *et al.* Regulation of FAS exon definition and apoptosis by the Ewing
1070 sarcoma protein. *Cell Rep.* **7**, 1211–1226 (2014).

1071 35. Izquierdo, J. M. *et al.* Regulation of Fas alternative splicing by antagonistic effects of
1072 TIA-1 and PTB on exon definition. *Mol. Cell* **19**, 475–484 (2005).

1073 36. Choi, N. *et al.* SRSF6 Regulates the Alternative Splicing of the Apoptotic Fas Gene by
1074 Targeting a Novel RNA Sequence. *Cancers* **14**, (2022).

1075 37. Berget, S. M. Exon recognition in vertebrate splicing. *J. Biol. Chem.* **270**, 2411–2414
1076 (1995).

1077 38. Ule, J. & Blencowe, B. J. Alternative Splicing Regulatory Networks: Functions,
1078 Mechanisms, and Evolution. *Mol. Cell* **76**, 329–345 (2019).

1079 39. Dominski, Z. & Kole, R. Selection of splice sites in pre-mRNAs with short internal exons.
1080 *Mol. Cell. Biol.* **11**, 6075–6083 (1991).

1081 40. Irimia, M. *et al.* A highly conserved program of neuronal microexons is misregulated in
1082 autistic brains. *Cell* **159**, 1511–1523 (2014).

1083 41. Juan-Mateu, J. *et al.* Pancreatic microexons regulate islet function and glucose
1084 homeostasis. *Nat Metab* **5**, 219–236 (2023).

1085 42. Gao, K., Masuda, A., Matsuura, T. & Ohno, K. Human branch point consensus
1086 sequence is yUnAy. *Nucleic Acids Res.* **36**, 2257–2267 (2008).

1087 43. Izquierdo, J. M. & Valcárcel, J. Fas-activated serine/threonine kinase (FAST K)
1088 synergizes with TIA-1/TIAR proteins to regulate Fas alternative splicing. *J. Biol. Chem.*
1089 **282**, 1539–1543 (2007).

1090 44. Singh, R., Valcárcel, J. & Green, M. R. Distinct binding specificities and functions of
1091 higher eukaryotic polypyrimidine tract-binding proteins. *Science* **268**, 1173–1176 (1995).

1092 45. Gonatopoulos-Pournatzis, T. *et al.* Genome-wide CRISPR-Cas9 Interrogation of
1093 Splicing Networks Reveals a Mechanism for Recognition of Autism-Misregulated
1094 Neuronal Microexons. *Mol. Cell* **72**, 510–524.e12 (2018).

1095 46. Förch, P. *et al.* The apoptosis-promoting factor TIA-1 is a regulator of alternative pre-
1096 mRNA splicing. *Mol. Cell* **6**, 1089–1098 (2000).

1097 47. Schott, G. *et al.* U2AF2 binds IL7R exon 6 ectopically and represses its inclusion. *RNA*
1098 **27**, 571–583 (2021).

1099 48. Corvelo, A., Hallegger, M., Smith, C. W. J. & Eyras, E. Genome-wide association
1100 between branch point properties and alternative splicing. *PLoS Comput. Biol.* **6**,
1101 e1001016 (2010).

1102 49. Weng, L. *et al.* A novel alternative spliced chondrolectin isoform lacking the
1103 transmembrane domain is expressed during T cell maturation. *J. Biol. Chem.* **278**,
1104 19164–19170 (2003).

1105 50. Excoffon, K. J. D. A., Bowers, J. R. & Sharma, P. I. Alternative splicing of viral
1106 receptors: A review of the diverse morphologies and physiologies of adenoviral
1107 receptors. *Recent Res Dev Viro* **9**, 1–24 (2014).

1108 51. Rosenberg, A. B., Patwardhan, R. P., Shendure, J. & Seelig, G. Learning the sequence
1109 determinants of alternative splicing from millions of random sequences. *Cell* **163**, 698–
1110 711 (2015).

1111 52. Cheng, J. *et al.* MMSplice: modular modeling improves the predictions of genetic variant
1112 effects on splicing. *Genome Biol.* **20**, 48 (2019).

1113 53. Jaganathan, K. *et al.* Predicting Splicing from Primary Sequence with Deep Learning.
1114 *Cell* **176**, 535–548.e24 (2019).

1115 54. Zeng, T. & Li, Y. I. Predicting RNA splicing from DNA sequence using Pangolin.
1116 *Genome Biol.* **23**, 103 (2022).

1117 55. Hall, K. B. RNA-protein interactions. *Curr. Opin. Struct. Biol.* **12**, 283–288 (2002).

1118 56. Ray, D. *et al.* A compendium of RNA-binding motifs for decoding gene regulation.
1119 *Nature* **499**, 172–177 (2013).

1120 57. Pan, X., Rijnbeek, P., Yan, J. & Shen, H.-B. Prediction of RNA-protein sequence and
1121 structure binding preferences using deep convolutional and recurrent neural networks.
1122 *BMC Genomics* **19**, 511 (2018).

1123 58. Schaal, T. D. & Maniatis, T. Multiple distinct splicing enhancers in the protein-coding
1124 sequences of a constitutively spliced pre-mRNA. *Mol. Cell. Biol.* **19**, 261–273 (1999).

1125 59. Fairbrother, W. G., Yeh, R.-F., Sharp, P. A. & Burge, C. B. Predictive identification of
1126 exonic splicing enhancers in human genes. *Science* **297**, 1007–1013 (2002).

1127 60. Senapathy, P., Shapiro, M. B. & Harris, N. L. Splice junctions, branch point sites, and
1128 exons: sequence statistics, identification, and applications to genome project. *Methods
1129 Enzymol.* **183**, 252–278 (1990).

1130 61. Sorek, R. & Ast, G. Intronic sequences flanking alternatively spliced exons are
1131 conserved between human and mouse. *Genome Res.* **13**, 1631–1637 (2003).

1132 62. Zheng, C. L., Fu, X.-D. & Grabskov, M. Characteristics and regulatory elements defining
1133 constitutive splicing and different modes of alternative splicing in human and mouse.
1134 *RNA* **11**, 1777–1787 (2005).

1135 63. Havens, M. A. & Hastings, M. L. Splice-switching antisense oligonucleotides as
1136 therapeutic drugs. *Nucleic Acids Res.* **44**, 6549–6563 (2016).

1137 64. Faure, A. J., Schmiedel, J. M., Baeza-Centurion, P. & Lehner, B. DiMSum: an error
1138 model and pipeline for analyzing deep mutational scanning data and diagnosing
1139 common experimental pathologies. *Genome Biol.* **21**, 207 (2020).

1140 65. Baeza-Centurion, P., Miñana, B., Schmiedel, J. M., Valcárcel, J. & Lehner, B.
1141 Combinatorial Genetics Reveals a Scaling Law for the Effects of Mutations on Splicing.
1142 *Cell* **176**, 549–563.e23 (2019).

1143 66. Saraiva-Agostinho, N. & Barbosa-Morais, N. L. psichomics: graphical application for
1144 alternative splicing quantification and analysis. *Nucleic Acids Res.* **47**, e7 (2019).

1145 67. Dönmez, G., Hartmuth, K., Kastner, B., Will, C. L. & Lührmann, R. The 5' end of U2
1146 snRNA is in close proximity to U1 and functional sites of the pre-mRNA in early
1147 spliceosomal complexes. *Mol. Cell* **25**, 399–411 (2007).

1148 68. Osorio, D., Rondon-Villarreal, P. & Torres, R. Peptides: A Package for Data Mining of
1149 Antimicrobial Peptides. *R J.* **7**, 4–14 (2015).

1150 69. Durinck, S., Spellman, P. T., Birney, E. & Huber, W. Mapping identifiers for the
1151 integration of genomic datasets with the R/Bioconductor package biomaRt. *Nat. Protoc.*
1152 **4**, 1184–1191 (2009).

1153

1154 **Figure legends**

1155

1156 **Figure 1. Deep indel mutagenesis of FAS exon 6**

1157 A. Plasmid library design.

1158 B. Experimental protocol of our massively-parallel splicing assay (MPSA).

1159 C. Correlation between PSI values from individual transfections and MPSA-derived PSI
1160 values.

1161 D. Distribution of PSI values for variants with 1-nucleotide (nt) mutations.

1162 E. Heatmaps displaying inclusion levels of 1-nt substitutions, deletions, and insertions.

1163 F. Correlation between PSI values for 1-nt deletions and substitutions at the same position.

1164 G. Correlation between PSI values for 1-nt insertions after a given position and substitutions
1165 at that position.

1166 H. Correlation between PSI values for 1-nt insertions after a given position and 1-nt deletions
1167 at the same position

1168

1169 **Figure 2. The effects of short indels on the inclusion of FAS exon 6**

1170 A. Heatmap showing inclusion values for short deletions (1-9 nt in length).

1171 B. Heatmap showing inclusion values for 2-nt insertions.

1172 C. Heatmap showing inclusion values for 3-nt insertions.

1173 D. Correlation between 2 (or 3) nt sequences ranked by the median PSI of exon variants in
1174 our library, with this sequence inserted, and their rank based on median PSI of exons
1175 containing 30 (or 20) such 2mers (or 3mers) in their sequence (GTEx adipose tissue).

1176 E. Distribution of PSI values in exons with a 3-nt insertion compared to the frequency of
1177 each nucleotide in the insertion.

1178 F. Distribution of PSI values in cassette exons (GTEx adipose tissue) relative to the
1179 percentage of each nucleotide present in the exon sequence.

1180

1181 **Figure 3. Deep indel mutagenesis of FAS exon 6 reveals the origin of novel
1182 microexons**

1183 A. Relationship between exon length and inclusion (black curve represents a constrained B-
1184 spline fit to rolling median PSI values, and the yellow shaded area indicates the rolling
1185 interquartile range of PSI values).

1186 B. Distribution of cassette exon inclusion values versus exon length (GTEx adipose tissue).

1187 C. Sequence of FAS exon 6 and surrounding intronic sequences.

1188 D. Hypothetical mechanisms explaining how our experimental assay could result in the
1189 detection of a microexon in our mutant library.

1190 E. RT-PCR analysis of FAS exon 6 inclusion for the WT exonic sequence, two variants with
1191 insertions that introduce an AG after exon position 40 and one variant with an insertion after
1192 exon position 40 that does not introduce an AG dinucleotide.

1193 F. Illustration showing the impact of a weak or strong 3' splice site before FAS exon 6 on the
1194 recognition, by the splicing machinery, of the exonic 3' splice-site-like sequence in the
1195 central region of the exon (followed by an AG insertion).

1196 G. RT-PCR analysis of FAS exon 6 inclusion in the presence of a weak or strong 3' splice
1197 site, for the WT exon and an exon with an insertion introducing an AG dinucleotide after
1198 exon position 40.

1199 H-I. RT-PCR analysis of FAS exon 6 inclusion upon overexpression of PTB (WT sequence
1200 and variant with an insertion introducing an AG dinucleotide after exon position 40).

1201 J-K. RT-PCR analysis of FAS exon 6 inclusion upon overexpression of SRRM4 (WT
1202 sequence and variant with an insertion introducing an AG dinucleotide after exon position
1203 40).
1204 L. Spliceosome assembly assays using the indicated fluorescently-labeled RNAs (wild type
1205 or mutant Fas exon 6 sequences) and HeLa nuclear extracts. The position of complexes
1206 assembling U2 snRNP (A complex) and hnRNP proteins (H complex) are indicated.
1207 M. Quantification of the ratio between A and H complexes for wild type (WT) and 3' ss-
1208 containing (AUG) mutant RNAs as in L. P value corresponds to a 2-tailed t-test from 20
1209 replicates with WT RNA, and 19 replicates with UAG-containing RNA.
1210 N. Distributions of PSI values for double-nucleotide substitutions targeting (i) neither of the
1211 putative exonic branchpoint adenines; (ii) the second putative exonic branchpoint adenine as
1212 well as another nucleotide in the exon; (iii) the first putative exonic branchpoint adenine as
1213 well as another nucleotide in the exon; (iv) both putative exonic branchpoint adenines. P
1214 values correspond to 2-tailed Wilcoxon tests with 16230 data points in the CTAAC group,
1215 544 data points in the CTAXCT group, 549 data points in the CTXACT group, and 9
1216 datapoints in the CTXXCT group. Boxplot boxes represent the median, the interquartile
1217 range, and the boxplot whiskers extend up to 1.5 times the interquartile range.
1218 O. Distribution of PSI values for insertions that either introduce (left) or do not introduce
1219 (right) an AG dinucleotide after exonic position 40. P value corresponds to a 2-tailed
1220 Wilcoxon test with 60 data points in the “no” group and 29 data points in the “yes”
1221 group. Boxplot boxes represent the median, the interquartile range, and the boxplot whiskers
1222 extend up to 1.5 times the interquartile range.
1223

1224 **Figure 4. The inclusion of short alternative exons encoding one-pass transmembrane**
1225 **helices is regulated by exonic 3' splice site-like sequences**

1226 A. Amino acid category encoded by each codon, categorized by the number of pyrimidines
1227 in the codon.
1228 B. Hydropathy score of exons categorized into different length groups, divided by whether
1229 they have an exonic sequence more or less similar to a 3' splice site than FAS exon 6.
1230 C. Inclusion of exons categorized into different length groups, divided by whether they have
1231 an exonic sequence more or less similar to a 3' splice site than FAS exon 6.
1232 D. Model for the regulation of alternative exons encoding a one-pass transmembrane helix.
1233 E. Hypothesis suggesting that 3' splice site-like sequences in alternative exons encoding
1234 transmembrane helices promote exon skipping.
1235 F. RT-PCR analysis of the inclusion of two alternative exons (CHODL exon 5 and CXADR
1236 exon 6) that each encode a one-pass transmembrane helix, including wild-type (WT)
1237 sequences and sequence variants with the putative branchpoint adenine mutated.
1238

1239 **Figure 5. Deep learning predicts the inclusion of variants in our deep indel**
1240 **mutagenesis library**

1241 A. Correlations between the inclusion levels of all variants in our library and their inclusion
1242 levels according to five different predictors (Substitutions n = 189, Deletion n = 1985,
1243 Insertion n = 5744).
1244 B. Lower triangle: Heatmap displaying inclusion levels of all deletion variants in our mutant
1245 library. Upper triangle: Heatmap showing inclusion levels of all deletion variants in our
1246 mutant library as predicted by SpliceAI.

1247 C. Left: Inclusion levels of all 1-6 nt long deletion variants along the sequence of FAS exon
1248 6. The yellow line represents a loess fit with a 95% confidence band. Right: Inclusion levels
1249 of the same variants as predicted by SpliceAI.

1250

1251 **Figure 6. Architecture of regulatory elements in alternatively spliced exons across the**
1252 **transcriptome**

1253 A. Distribution of absolute effect sizes of all 4mer deletions in the exome, as predicted by
1254 SpliceAI and split by exon PSI groups.

1255 B. Hidden Markov model (HMM) with three states (enhancer, silencer, neutral) used to
1256 model the splicing regulatory architecture of exons across the genome.

1257 C. Predicted regulatory architecture of FAS exon 6 based on our HMM.

1258 D. Distribution of exonic splicing enhancer and silencer lengths across the exome, as
1259 predicted by our HMM.

1260 E. Distribution of the three states of our model in the first and last 20 4mers of all exons
1261 under 100 nucleotides long.

1262 F. Ternary plot illustrating the relative composition of E/N/S states along the sequences of all
1263 18,551 exons in our dataset. The colour of each point corresponds to the exon's length.

1264 G. Ternary plot illustrating the relative composition of E/N/S states along the sequences of
1265 all 18,551 exons in our. The colour of each point corresponds to the exon's PSI value.

1266

1267 **Figure 7. Design of splicing-modulating antisense oligonucleotides**

1268 A. The activity of a splicing regulatory element (SRE) could be modulated by using an
1269 antisense oligonucleotide (AON) to basepair with this region (therefore sterically blocking
1270 any proteins that might bind to the SRE) or alternatively by deleting the SRE altogether.

1271 B. Correlation between the PSI values of nine FAS exon 6 variants with 21-nt deletions and
1272 the PSI values of WT FAS exon 6 with a 21-nt AON base pairing to the corresponding
1273 regions. Horizontal error bars represent the standard deviation of three replicates. Vertical
1274 error bars represent the standard error of the mean in our deep insertion mutagenesis
1275 library.

1276 C. Correlation between the Dango scores of the same nine FAS exon 6 variants as in panel
1277 B, and the PSI values of the WT FAS exon 6 with a 21-nt AON base pairing to the
1278 corresponding regions. Horizontal error bars represent the standard deviation of three
1279 replicates.

1280 D. Percentage of 21-nt deletions with Dango scores above the indicated thresholds as a
1281 function of exon length.

1282 E. Distribution of Dango scores as a function of exon length.

1283 F. Custom genome browser track displaying the Dango scores for FAS exon 6. The
1284 corresponding PSI values as measured experimentally in our deep mutagenesis assay are
1285 shown in the heatmap below, using the same colour scale as figure 5B.

1286

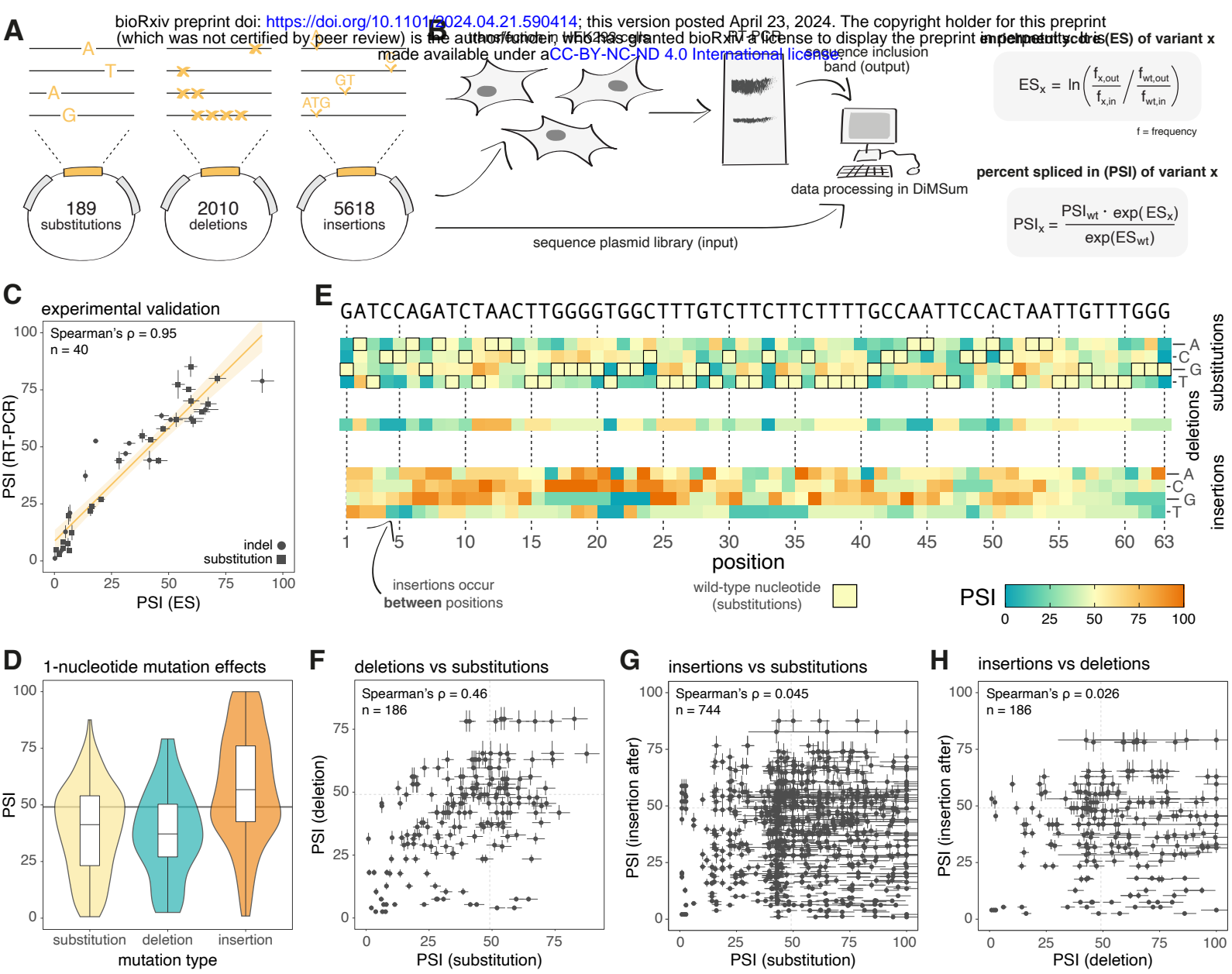


Figure 1

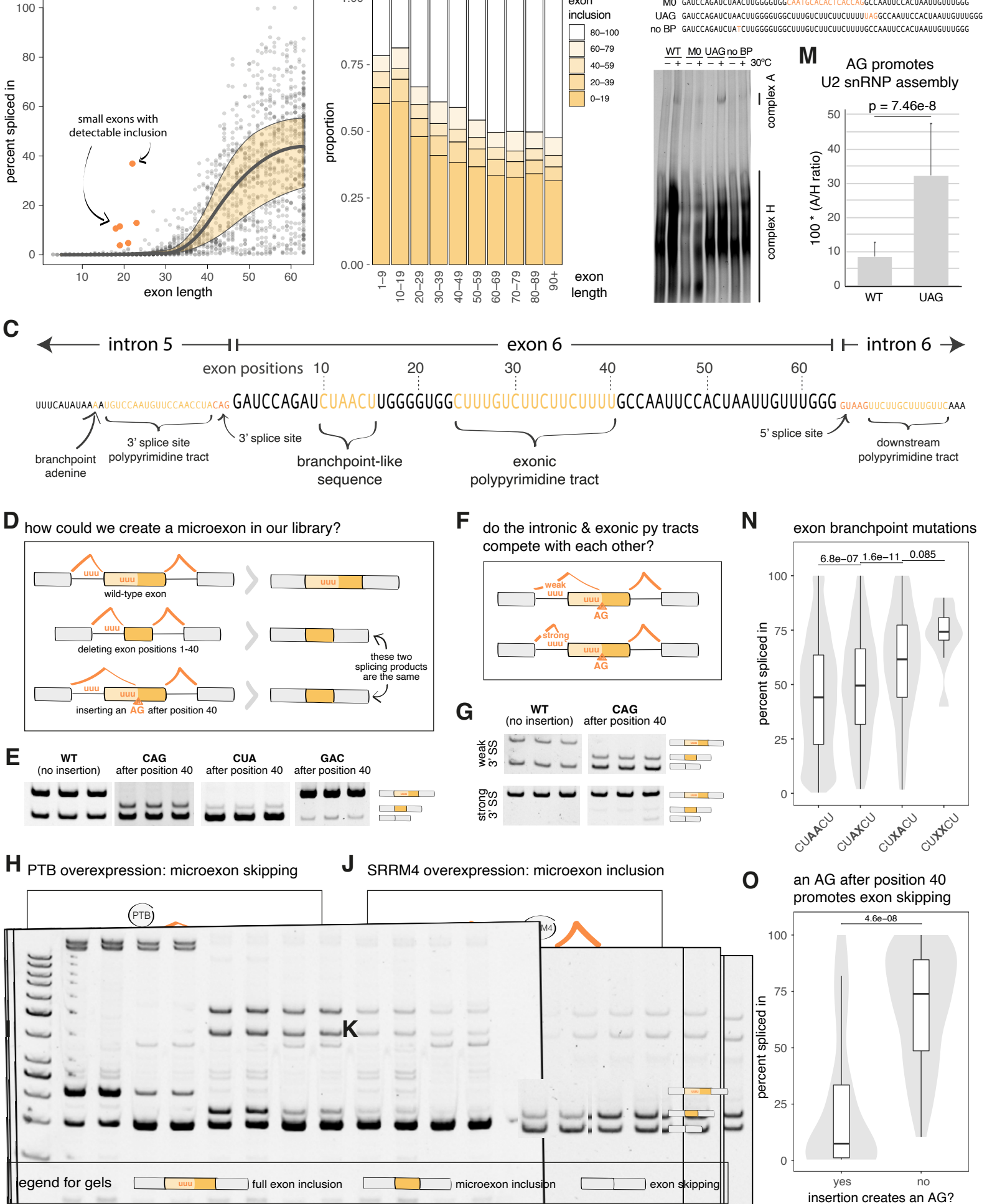


Figure 3

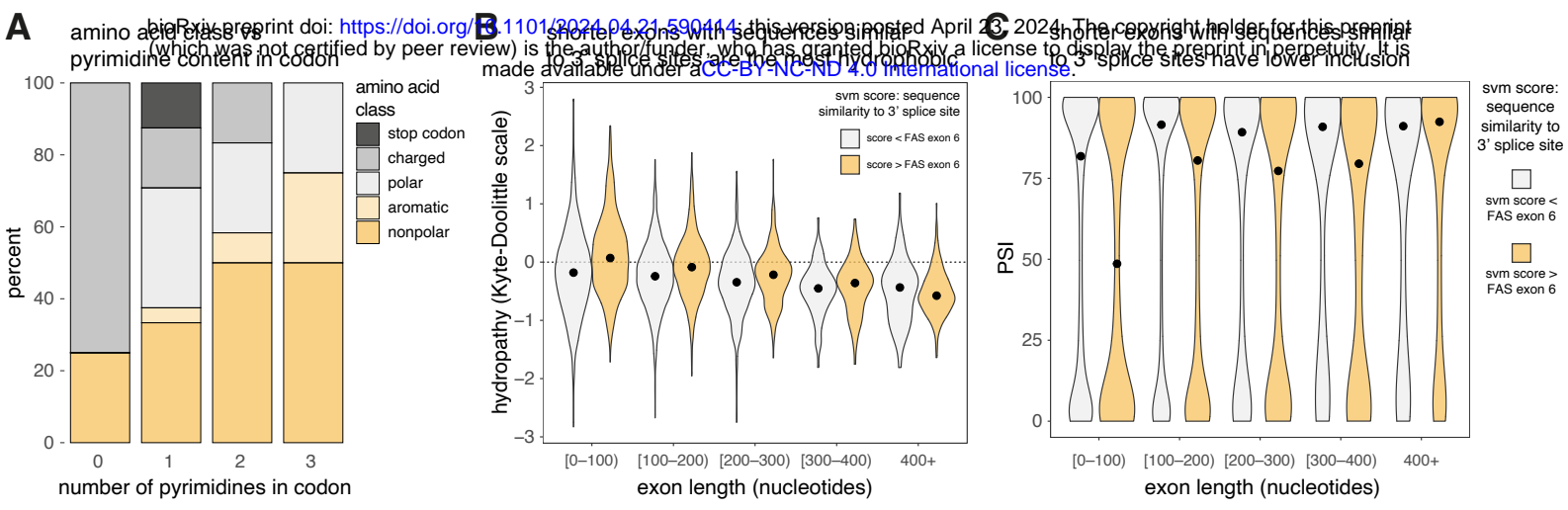
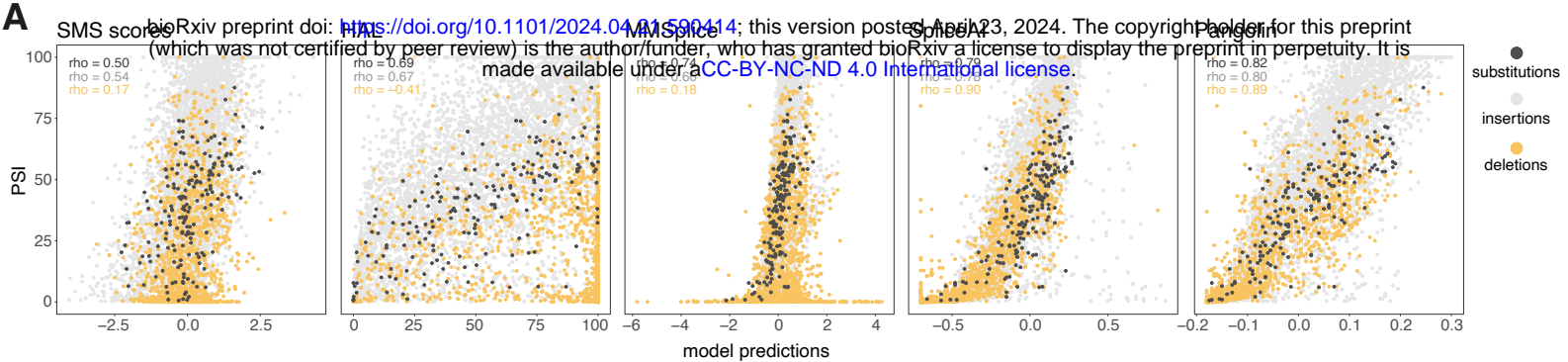


Figure 4



in silico mutagenesis of FAS exon 6

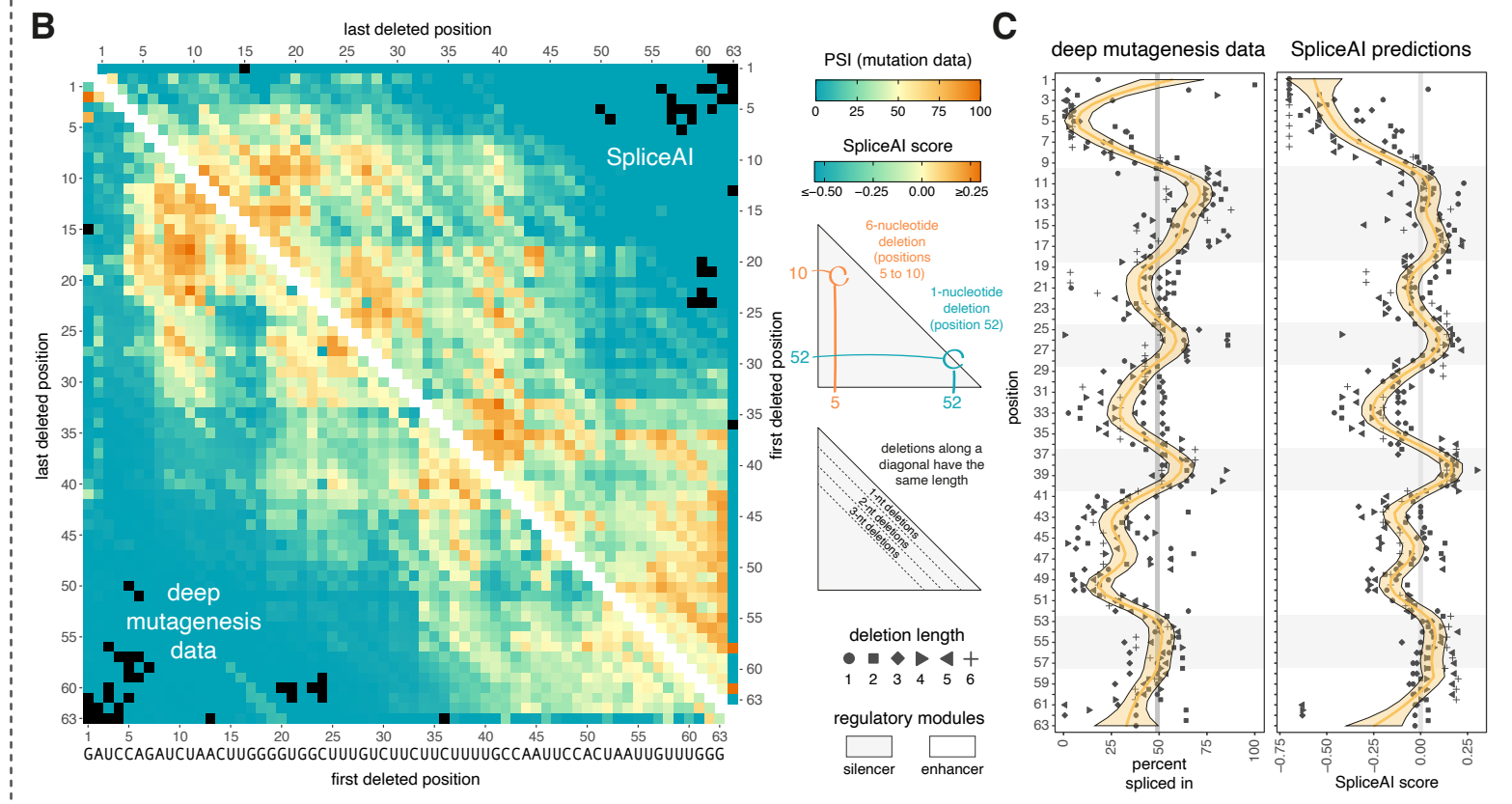


Figure 5

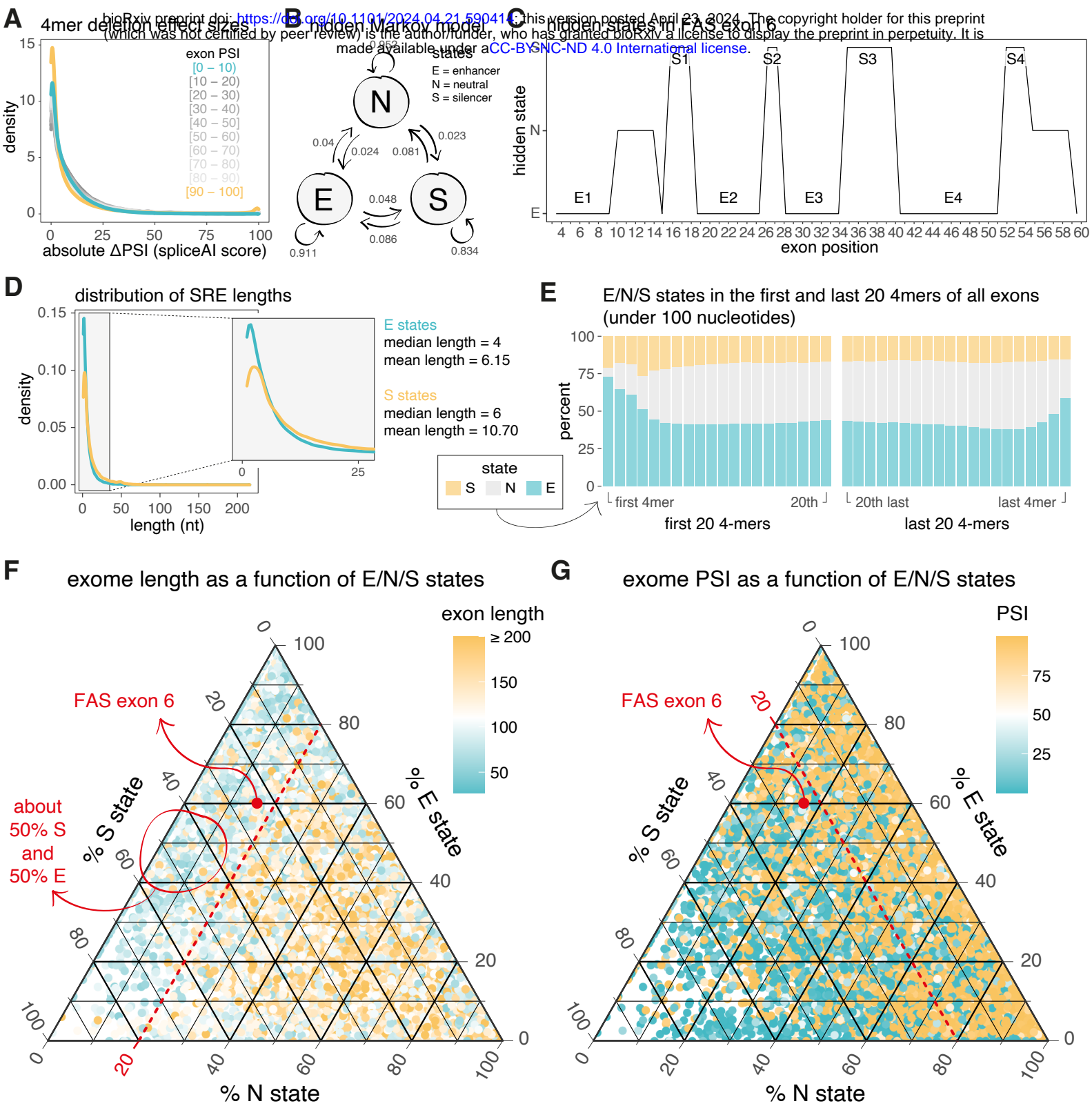


Figure 6

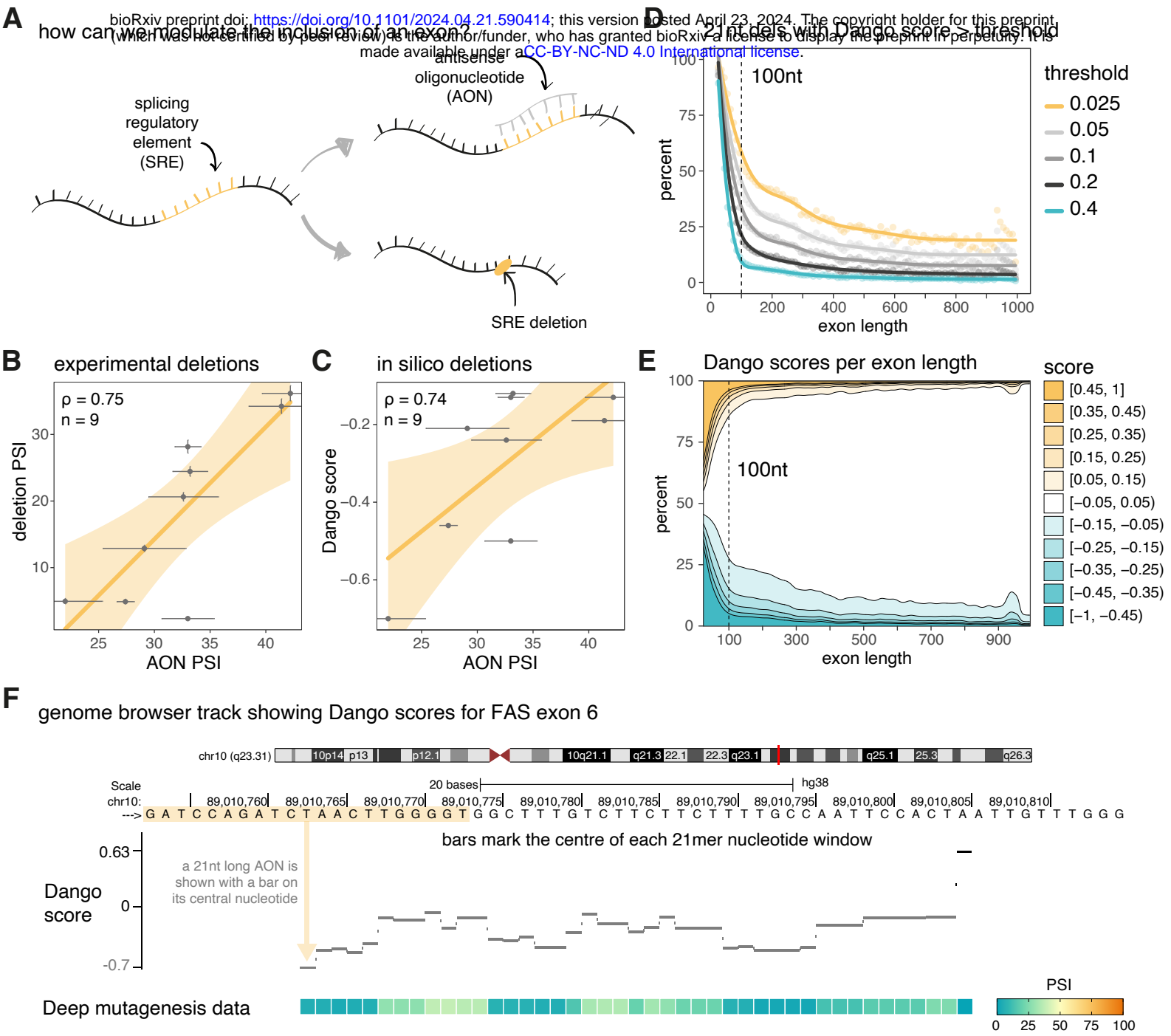
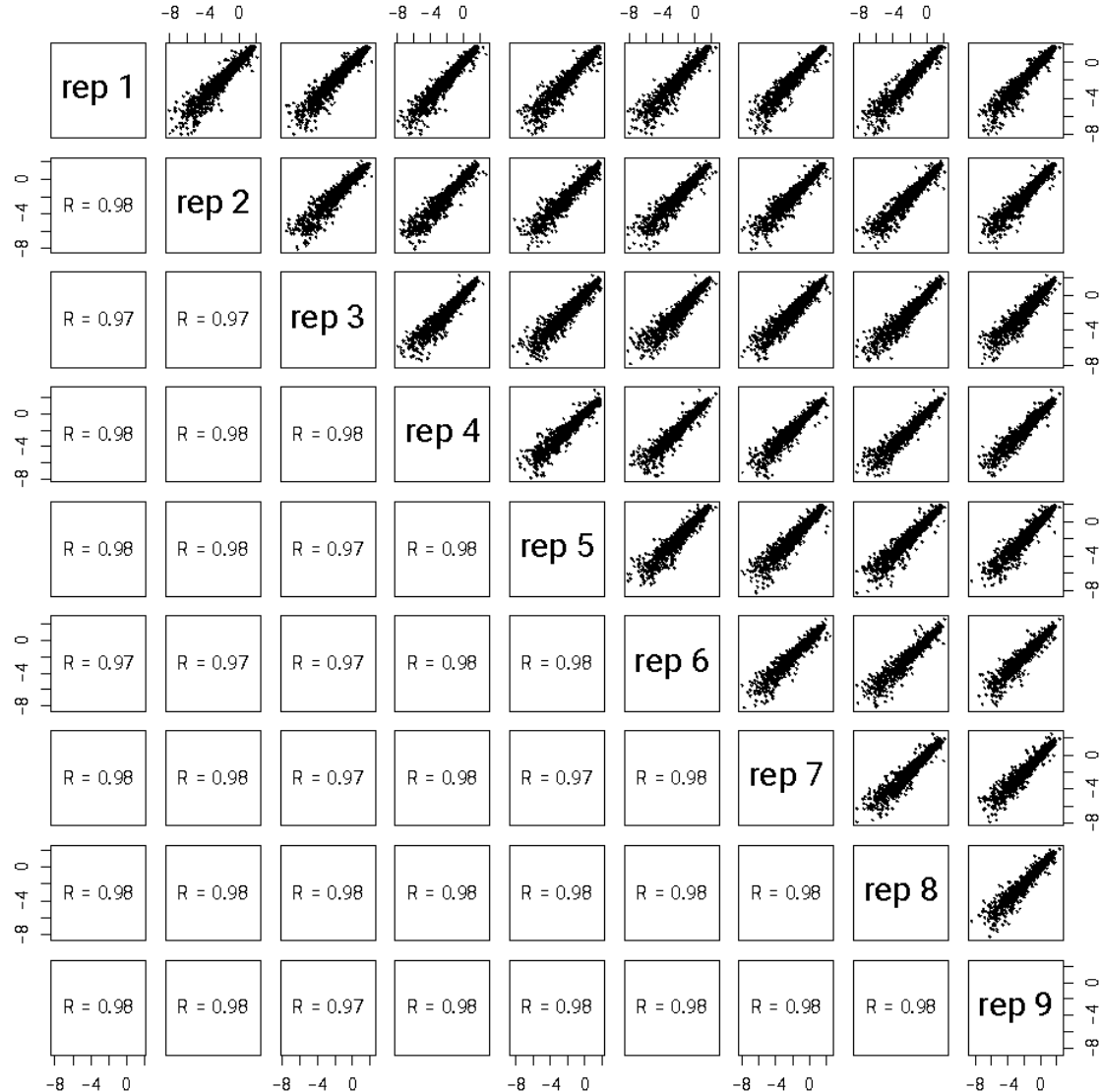


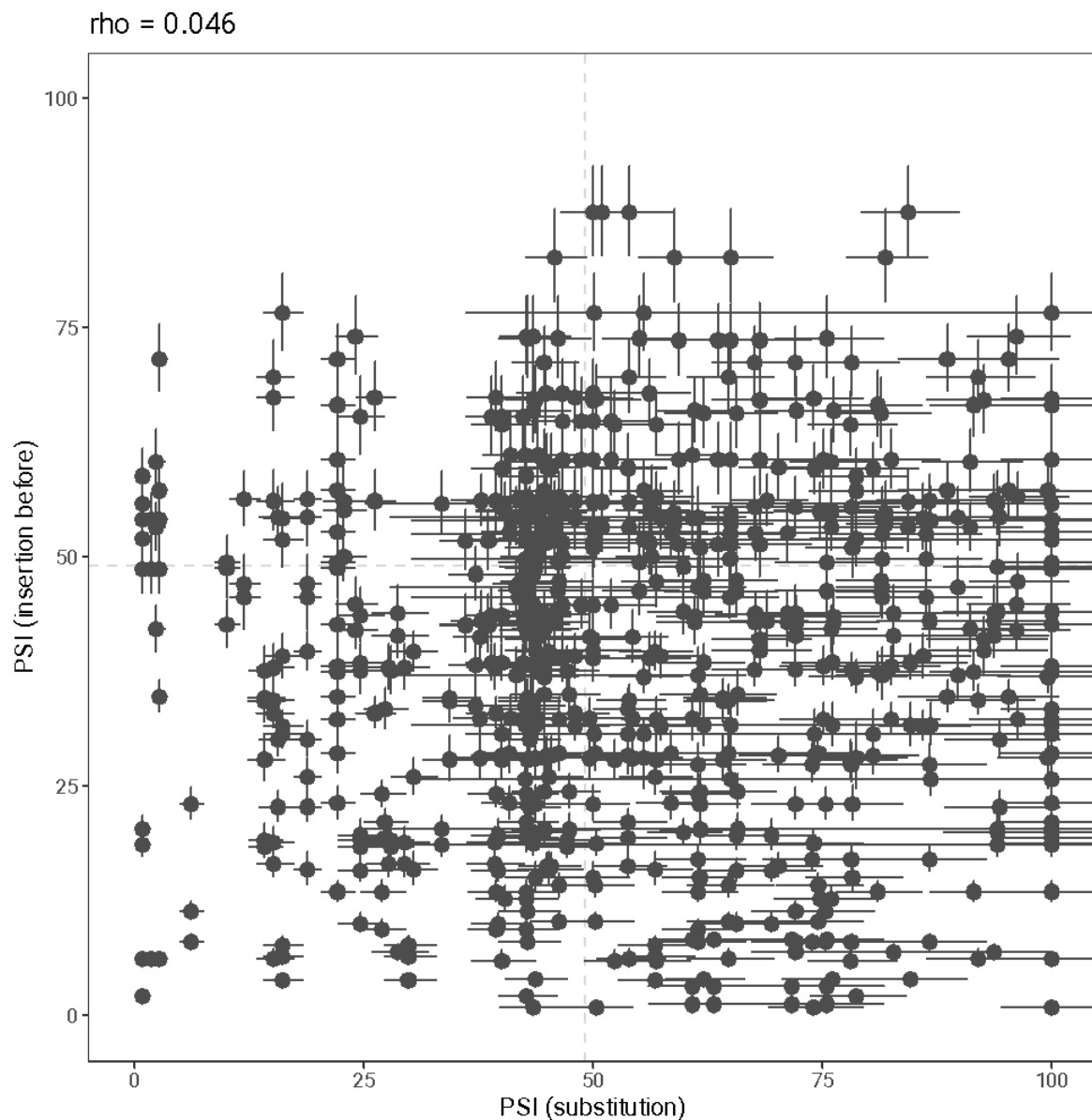
Figure 7

Figure S1



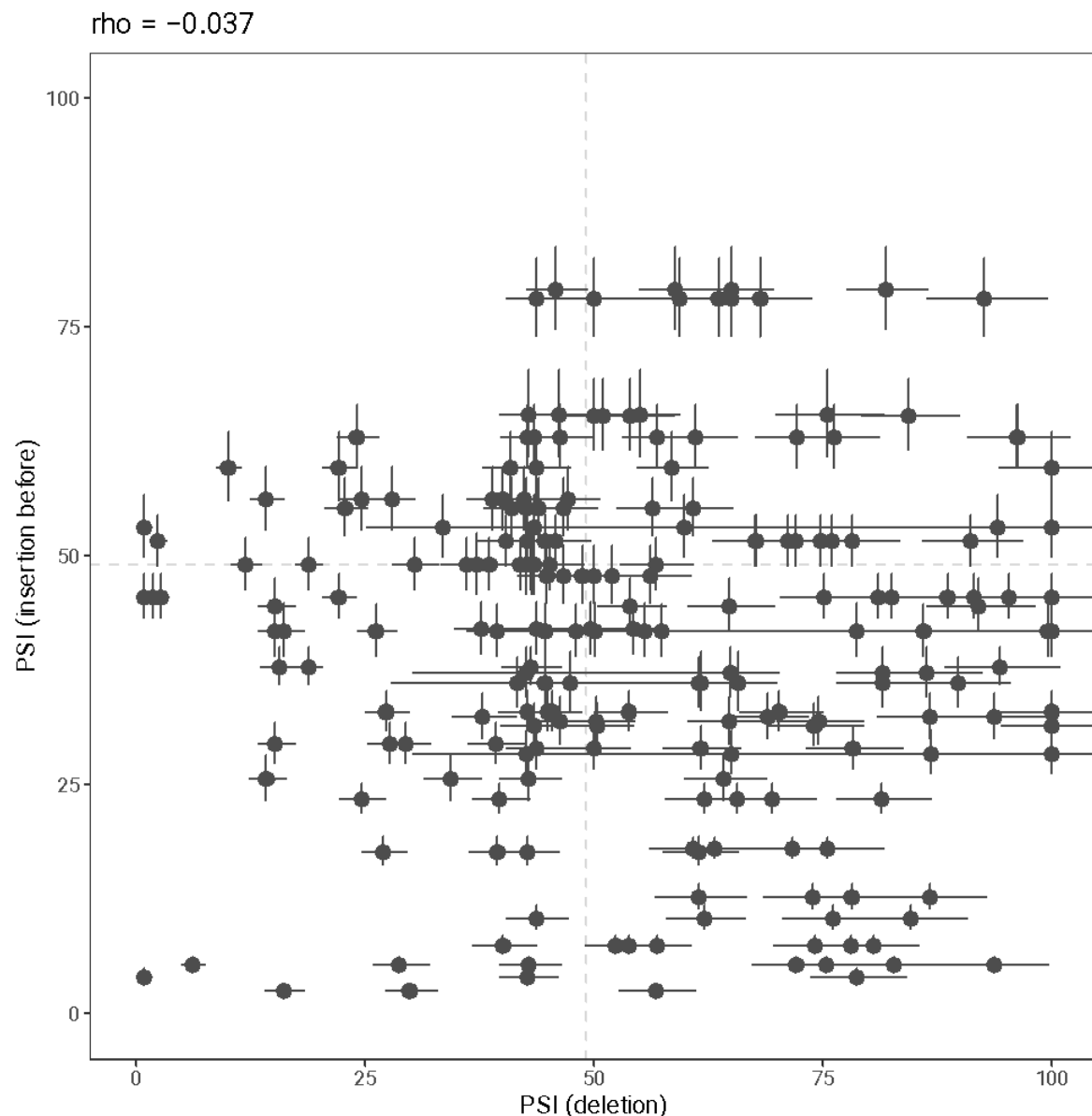
Pairwise correlations of enrichment scores for all exon variants in our library across nine experimental replicates.

Figure S2



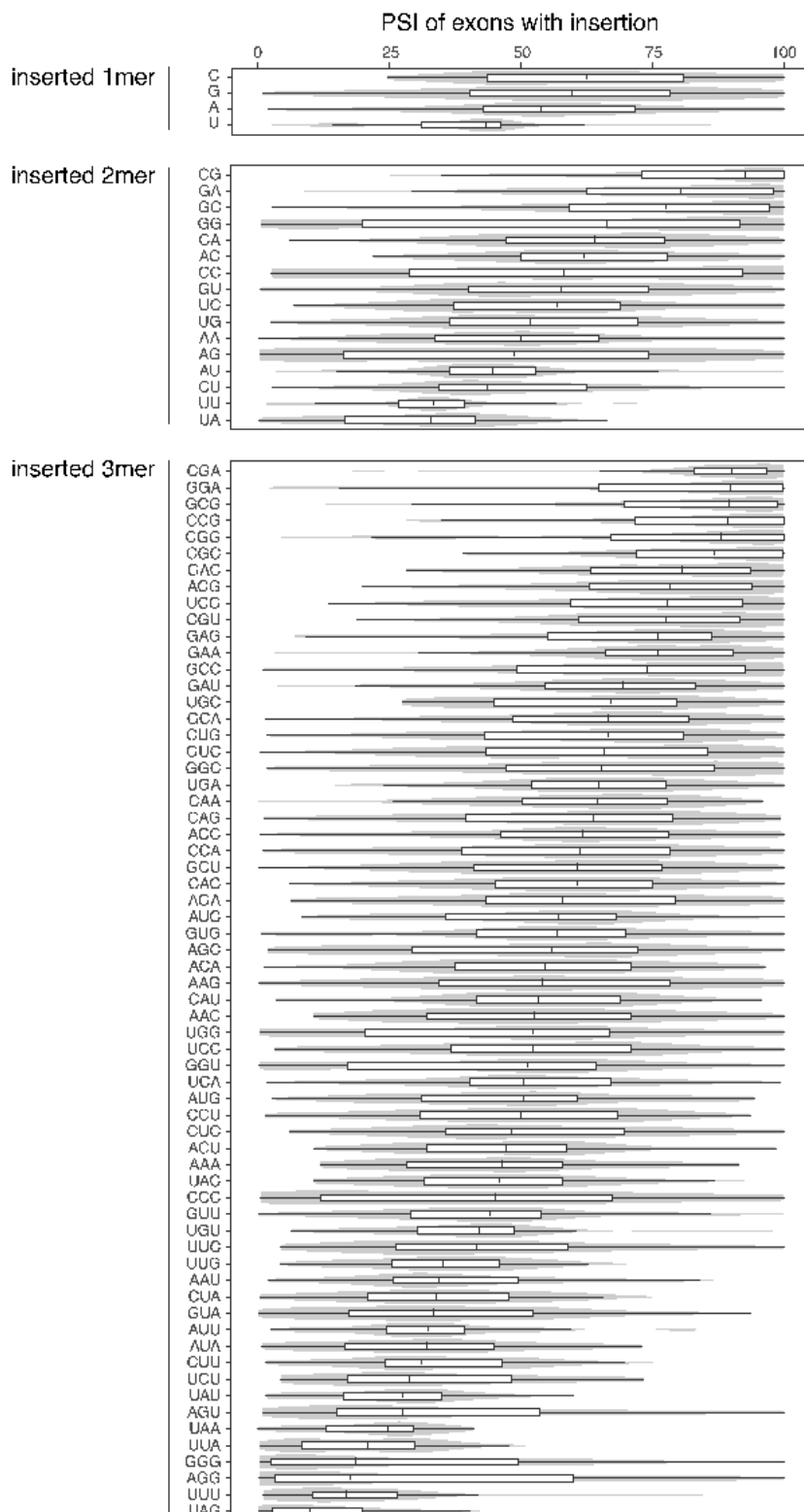
Correlation between PSI values for 1-nt insertions before a given position and substitutions at that position.

Figure S3



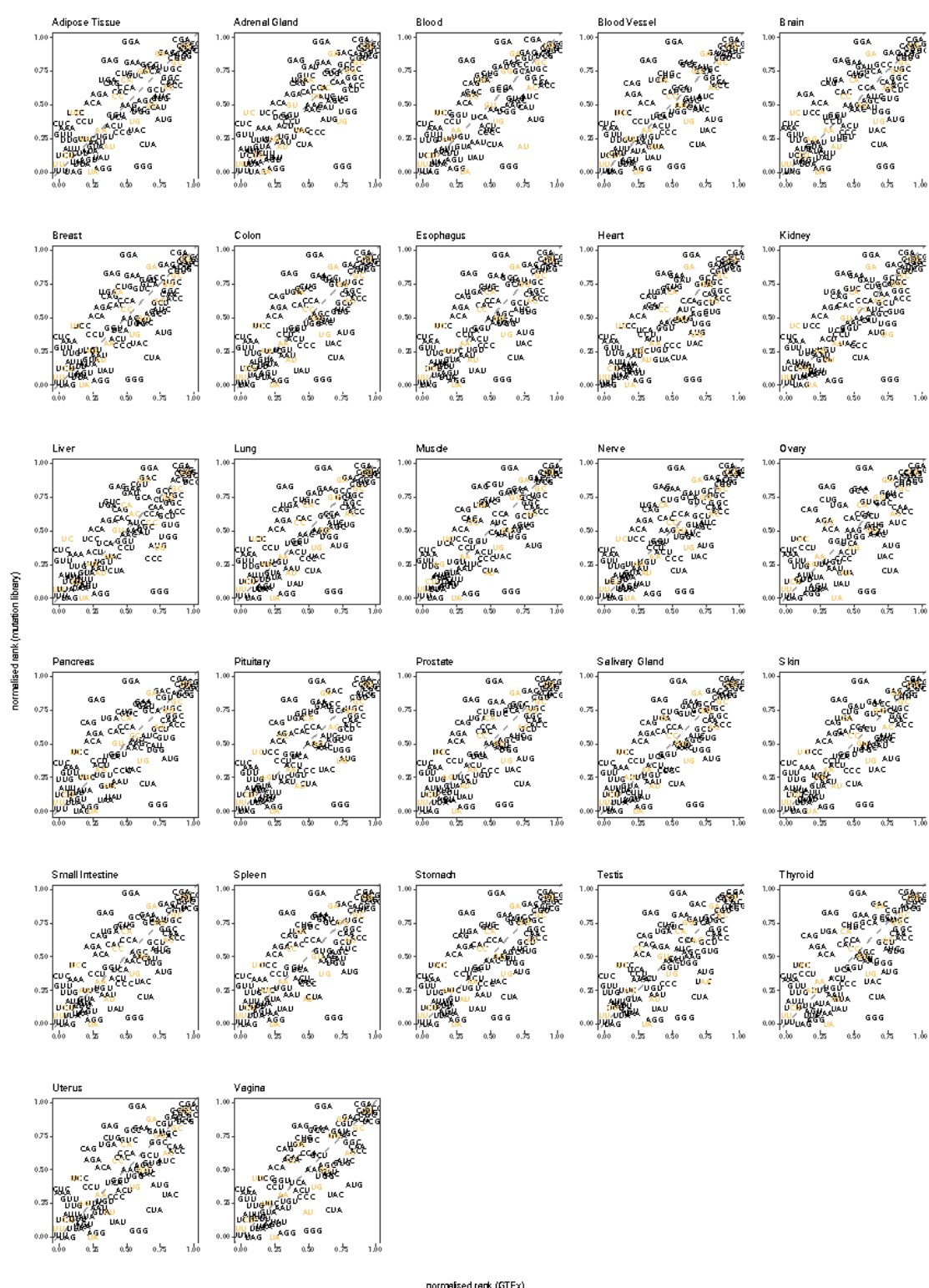
Correlation between PSI values for 1-nt insertions before a given position and deletions at that position.

Figure S4



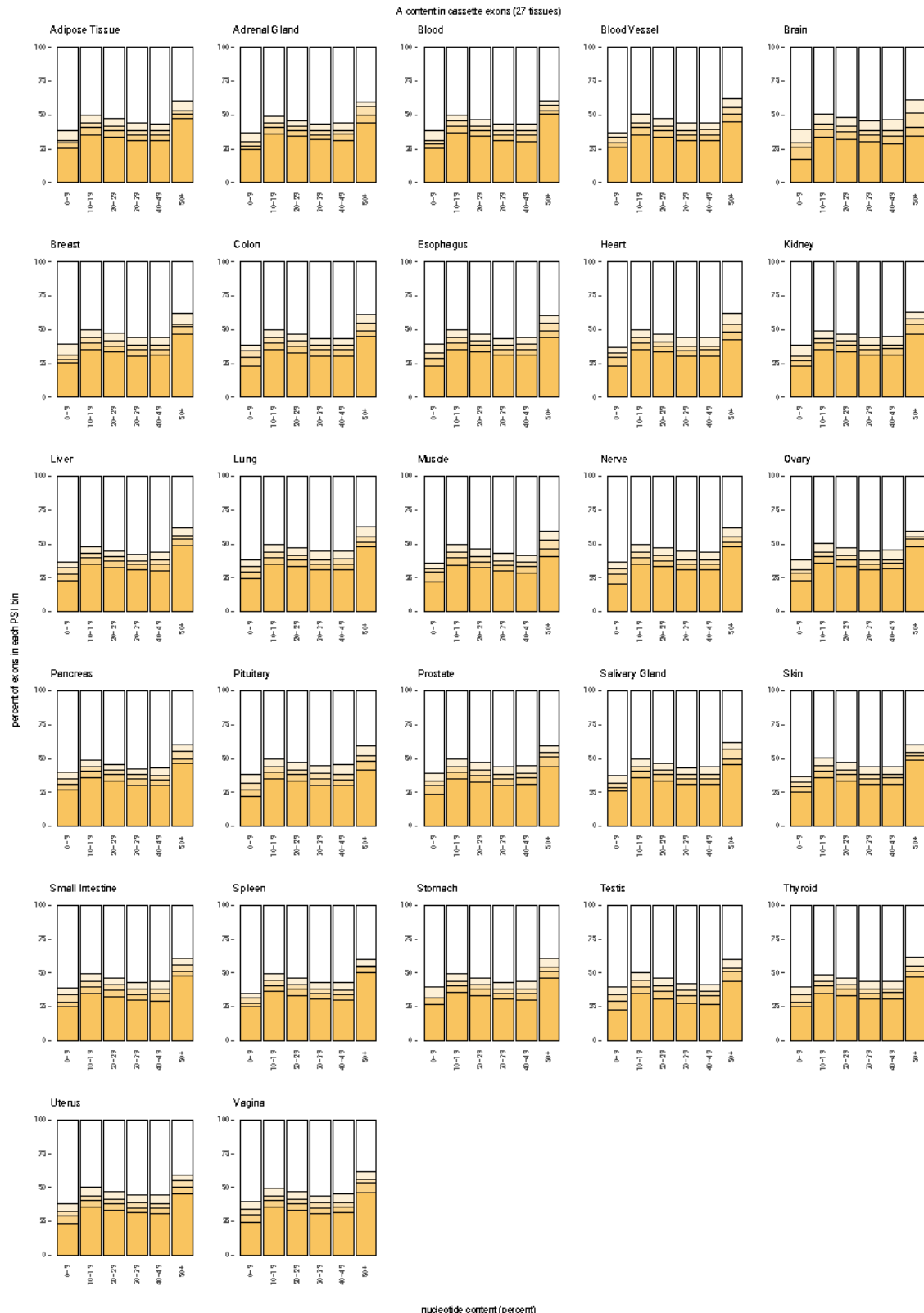
Distribution of inclusion values for exons with each possible 1-, 2-, and 3-nt insertion.

Figure S5



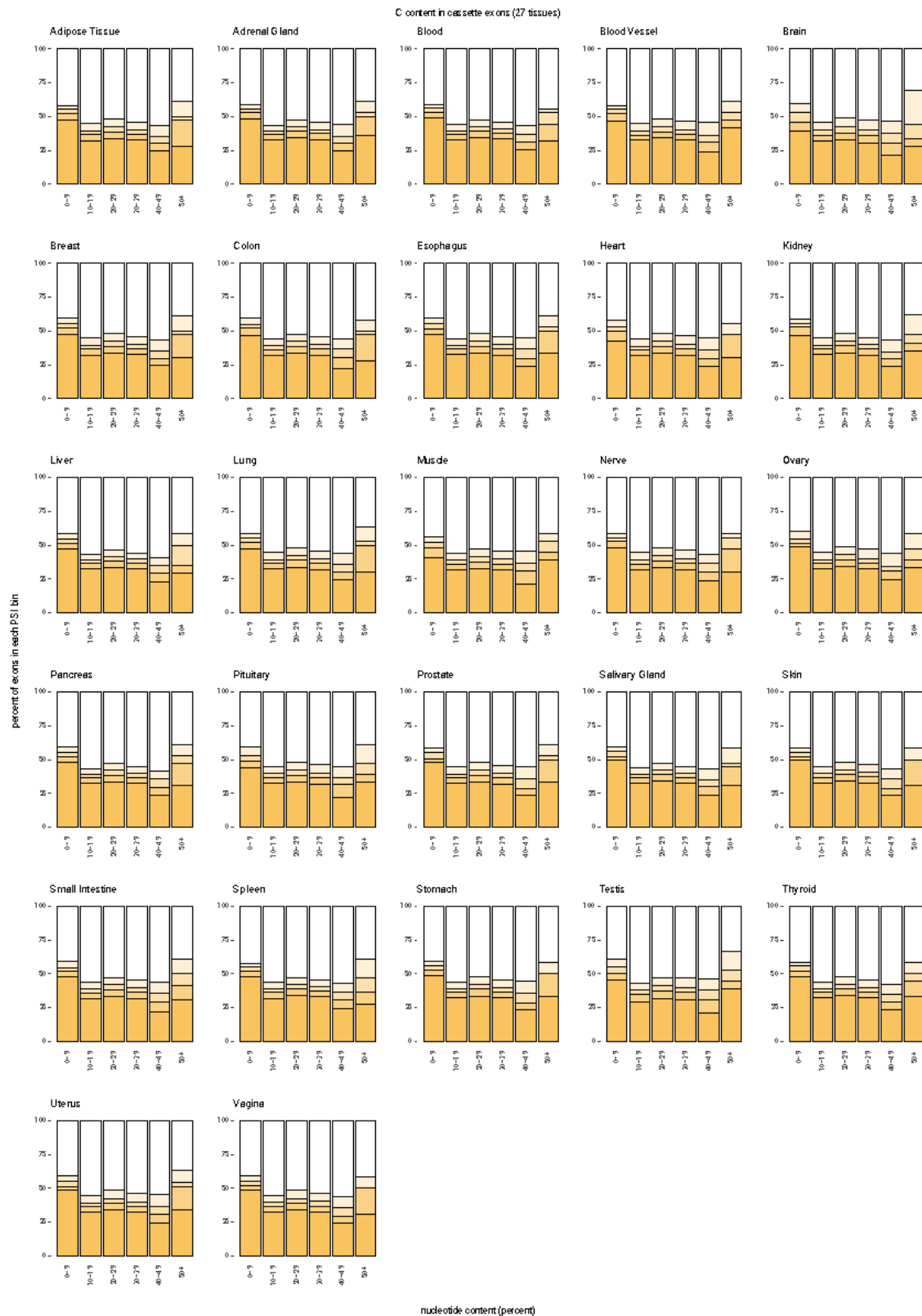
Correlation between 2 (or 3) nt sequences ranked by the median PSI of exon variants in our library, with this sequence inserted, and their rank based on median PSI of exons containing 30 (or 20) such 2mers (or 3mers) in their sequence (all GTEx tissues).

Figure S6



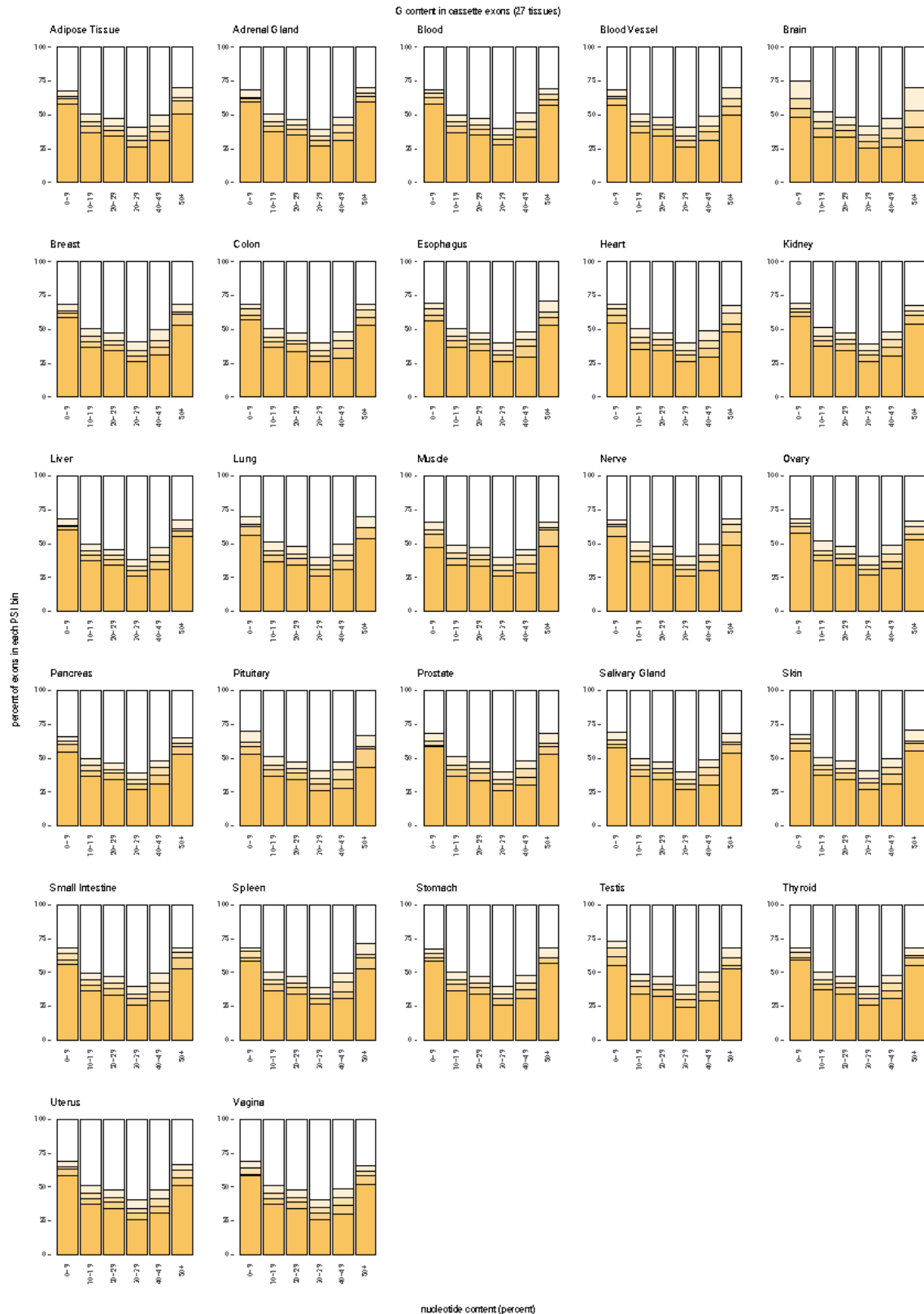
Distribution of PSI values in cassette exons (all GTEx tissues) relative to the percentage of each adenines present in the exon sequence.

Figure S7



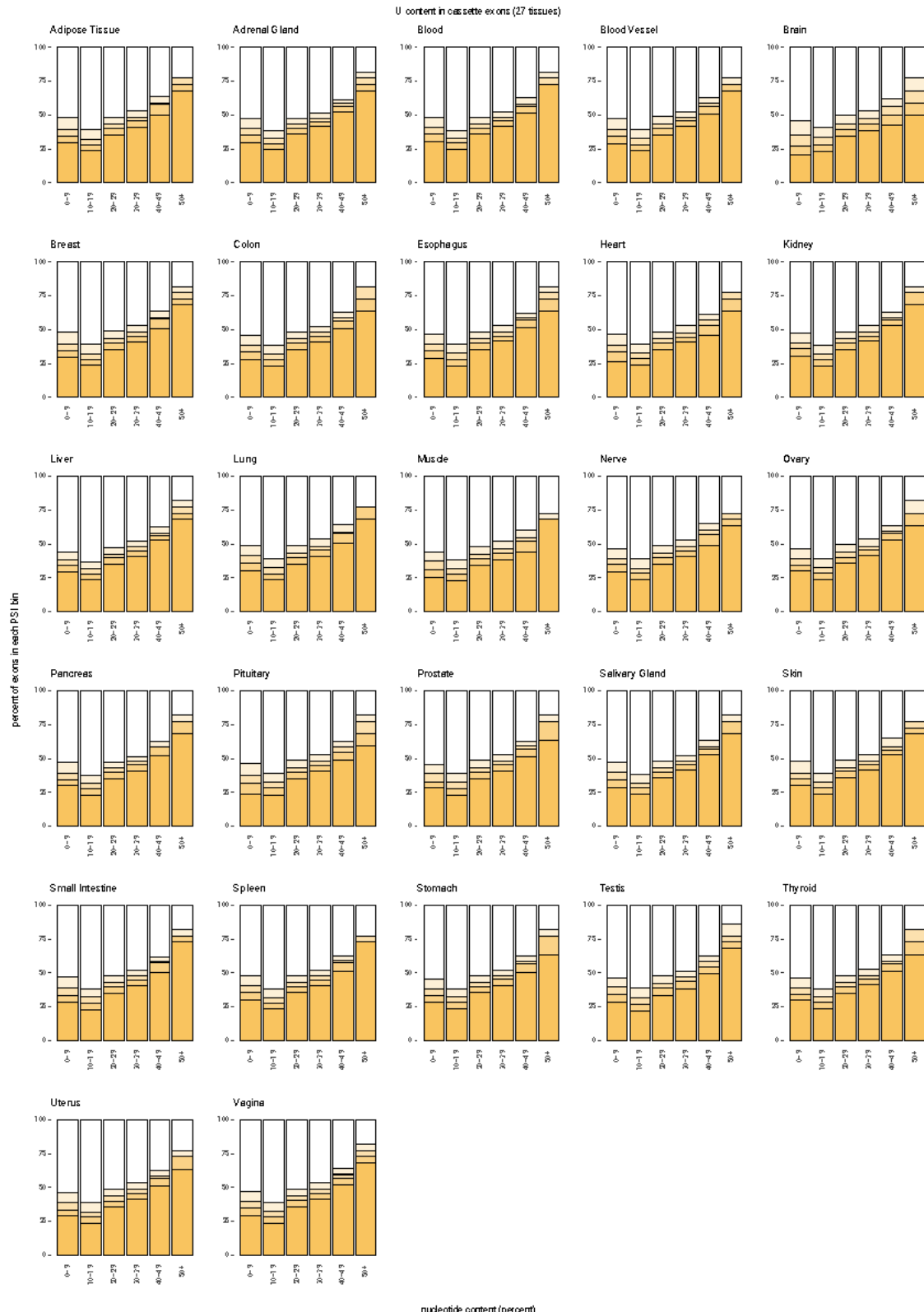
Distribution of PSI values in cassette exons (all GTEx tissues) relative to the percentage of each cytosines present in the exon sequence.

Figure S8



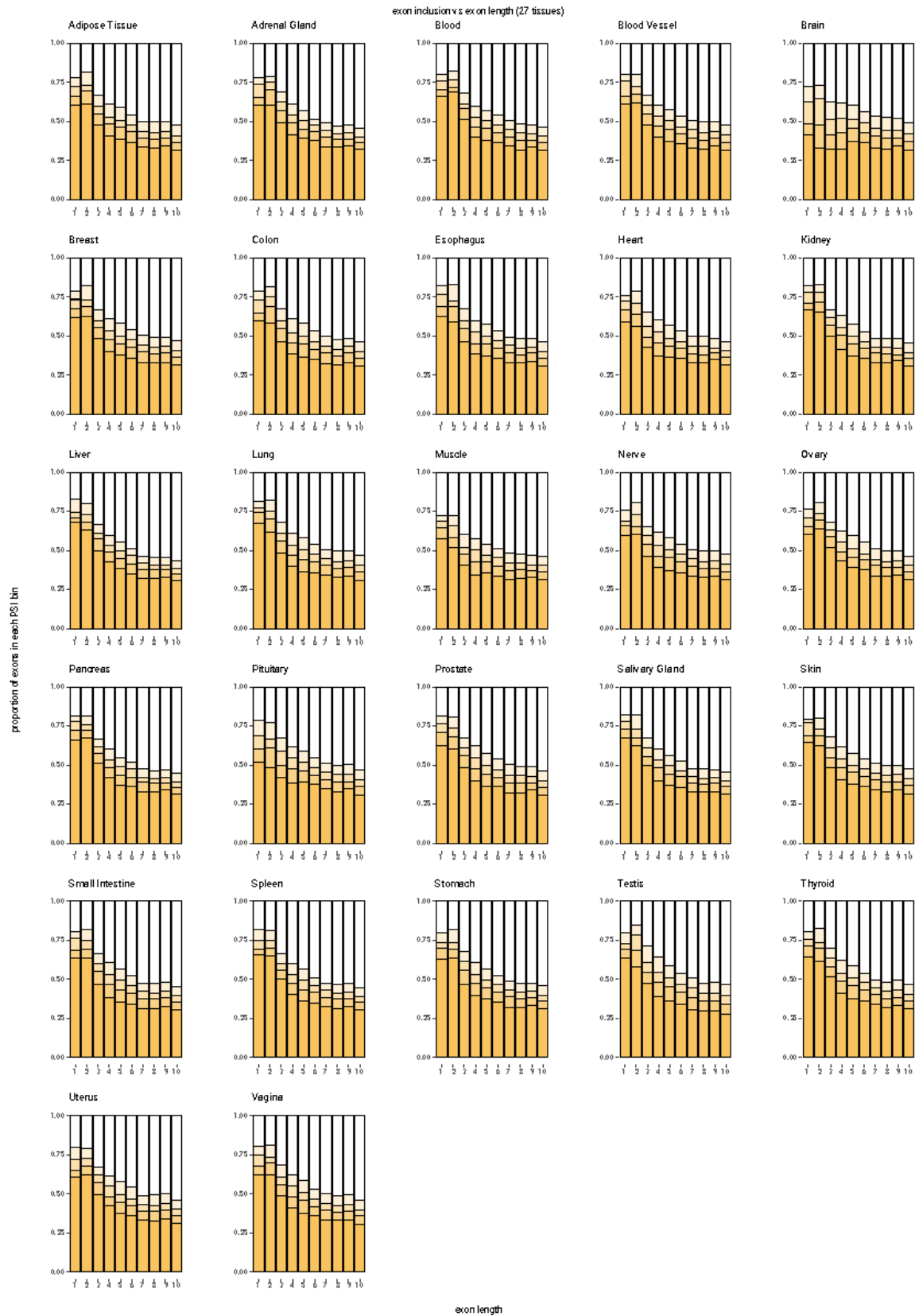
Distribution of PSI values in cassette exons (all GTEx tissues) relative to the percentage of each guanines present in the exon sequence.

Figure S9



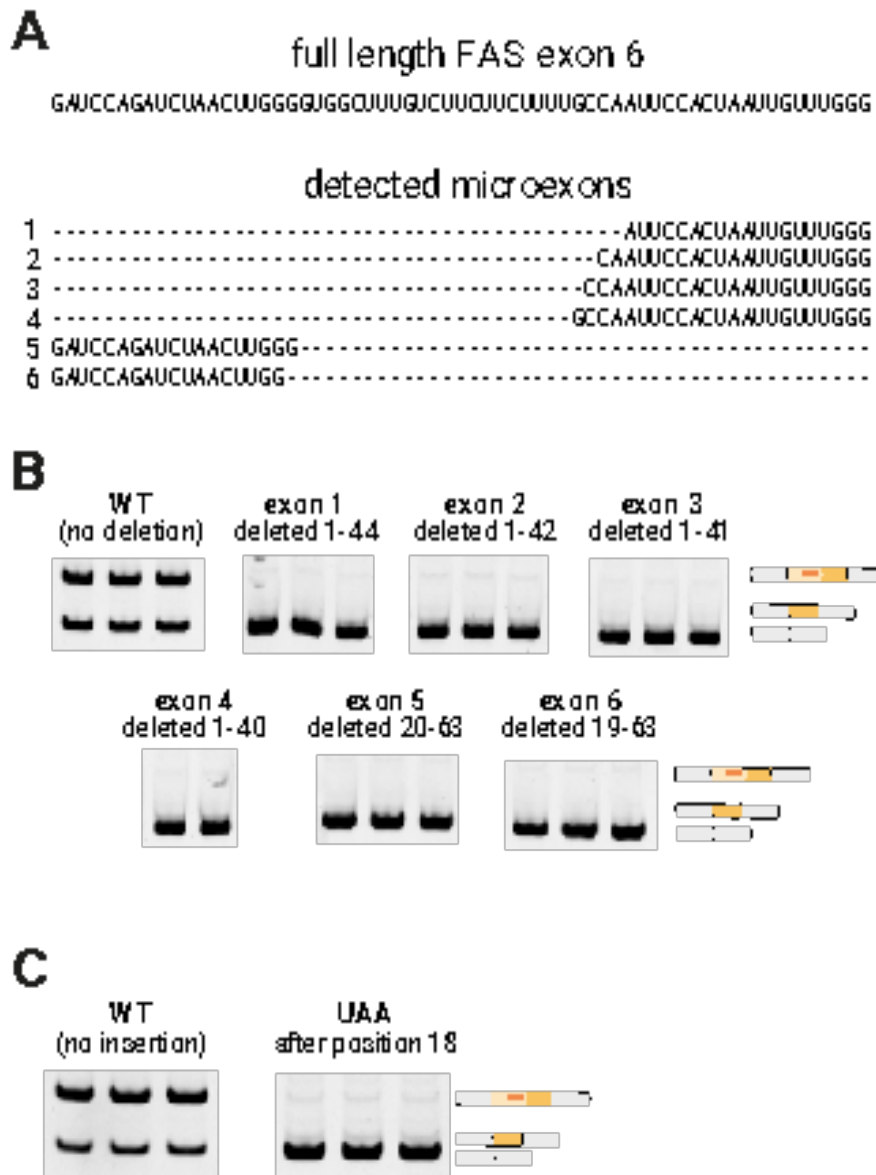
Distribution of PSI values in cassette exons (all GTEx tissues) relative to the percentage of each uracils present in the exon sequence.

Figure S10



Distribution of cassette exon inclusion values versus exon length (all GTEx tissues).

Figure S11



- A. Sequences of microexons in our library with detectable levels of inclusion.
- B. RT-PCR analysis of the inclusion of exons with a sequence corresponding to the detectable microexons.
- C. RT-PCR analysis of the inclusion of FAS exon 6 with a UAA insertion after exon position 18.

Figure S12

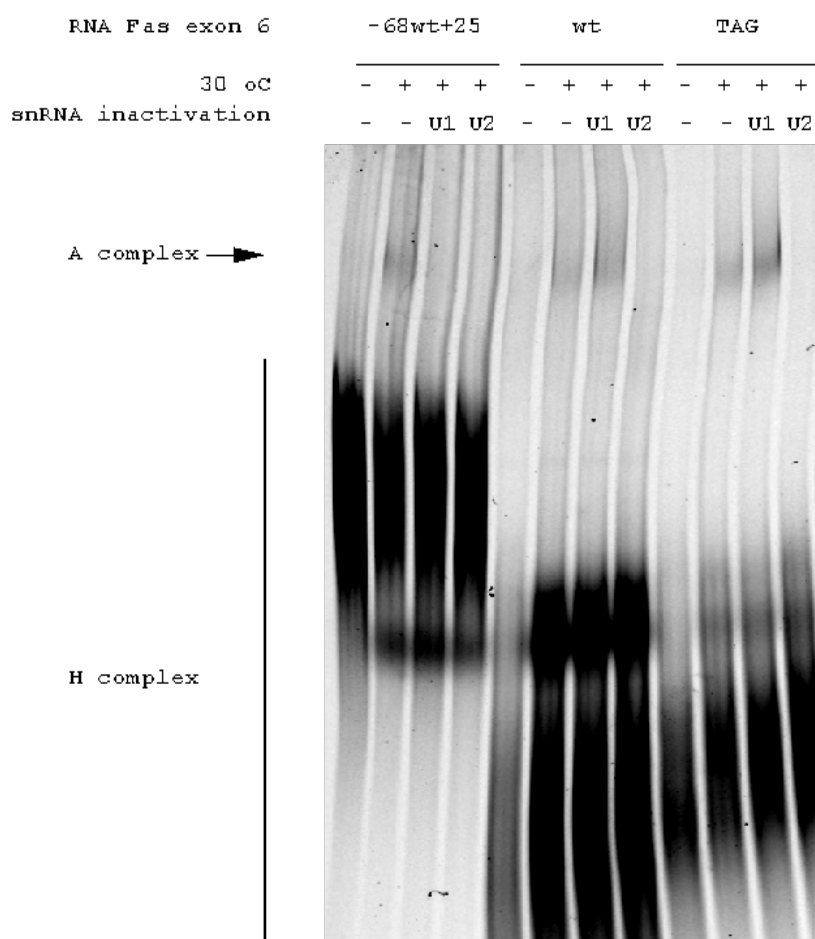


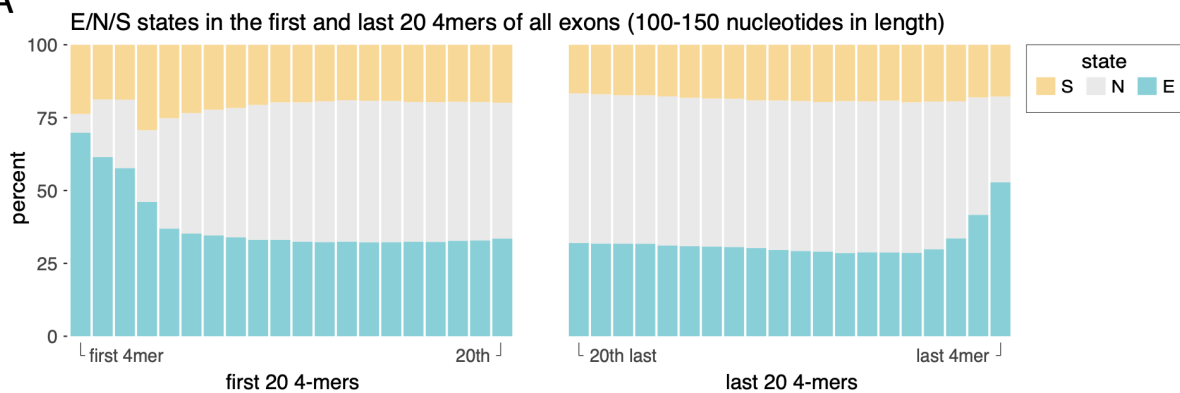
Figure S12. Validation of spliceosome assembly assays and enhanced A (U2 snRNP-containing) complex formation on Fas exon 6 upon inclusion of a 3' splice site (TAG).

Fluorescently-labeled RNAs corresponding to Fas exon 6 (wt), Fas exon 6 with a mutation that creates a 3' splice site after the internal polypyrimidine tract (TAG) (see Figure 3) or Fas exon 6 flanked by intronic sequences (-68wt+25, which includes the 3' 68 nucleotides of intron 5 and the 5' 25 nucleotides of intron 6) were incubated with HeLa nuclear extracts under in vitro splicing conditions at 30 C (+) or on ice as a control (-) and the ribonucleoprotein complexes formed were fractionated by electrophoresis on a composite agarose-polyacrylamide gel. The electrophoretic positions of U2 snRNP-containing complexes (A complex) and hnRNP-containing complexes (H complex) are indicated. Controls of U1 / U2 snRNP inactivation by RNase H-mediated digestion of the 5' end of U1 snRNA or of the branch point recognition sequence of U2 snRNA are included. Inactivation of U2 snRNP (but not of U1 snRNP) reduces A complex formation on WT and TAG RNAs, while complexes formed on the -68wt+25 RNA are sensitive to inactivation of either U1 or

U2 snRNPs because of exon definition-mediated effects (Izquierdo et al Mol Cell 19: 475-484, 2005). Note the significant increase in A/H complex ratio upon inclusion of a 3' splice site (TAG) in Fas exon 6 compared to the wild type sequence (WT).

Figure S13

A



B

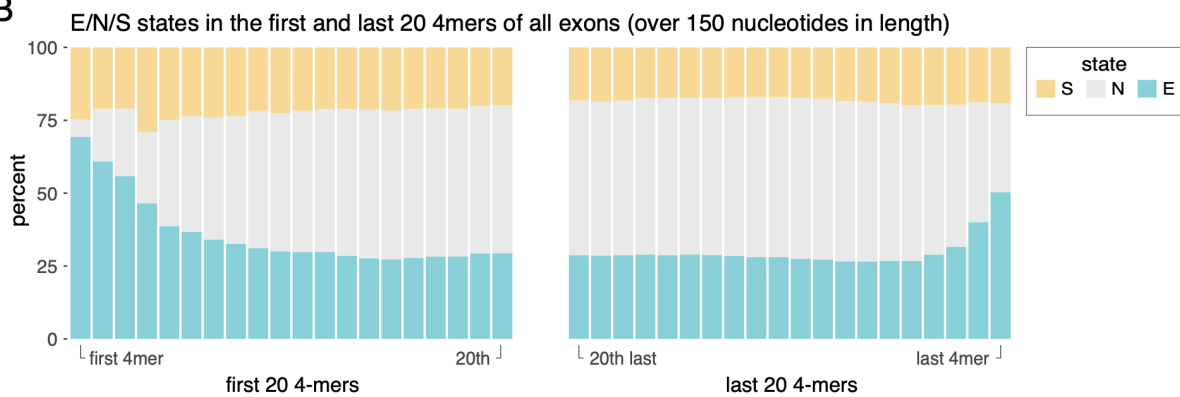
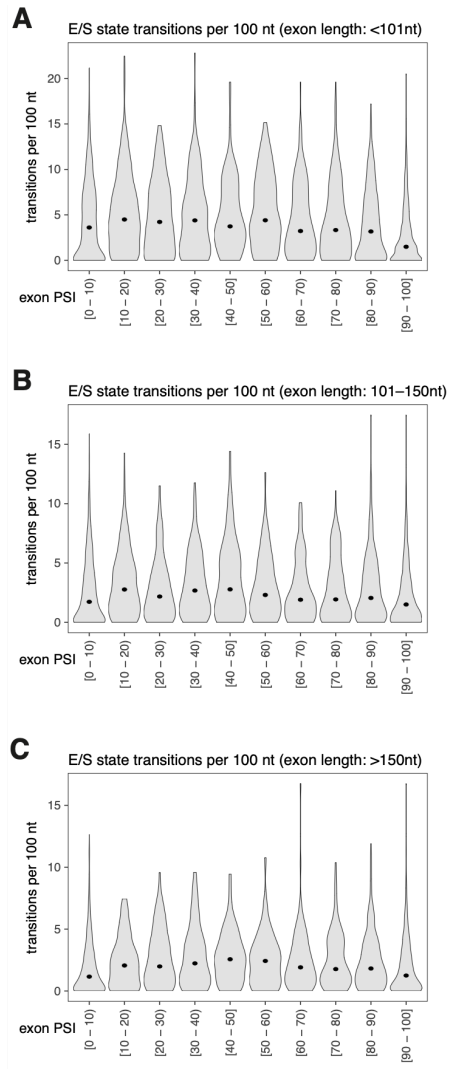


Figure S14

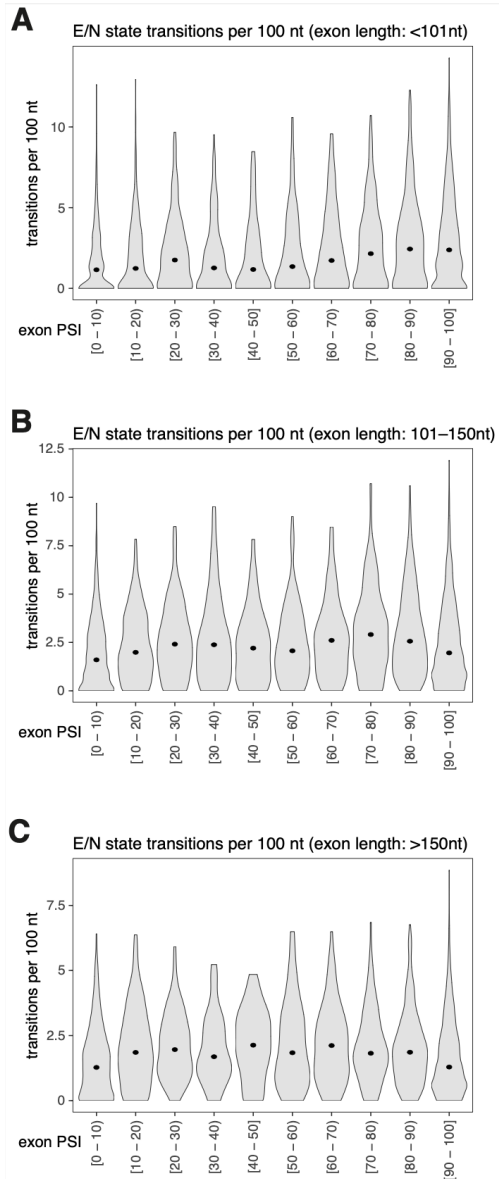


A. Distribution of the number of enhancer-silencer ("E"/"S") state transitions per 100 nucleotides in all exons shorter than 101 nt, divided into groups based on exon inclusion levels.

B. Distribution of the number of enhancer-silencer ("E"/"S") state transitions per 100 nucleotides in all exons with a length between 101 and 150 nt, divided into groups based on exon inclusion levels.

C. Distribution of the number of enhancer-silencer ("E"/"S") state transitions per 100 nucleotides in all exons longer than 150 nt, divided into groups based on exon inclusion levels.

Figure S15



A. Distribution of the number of enhancer-neutral ("E"/"N") state transitions per 100 nucleotides in all exons shorter than 101 nt, divided into groups based on exon inclusion levels.

B. Distribution of the number of enhancer-neutral ("E"/"N") state transitions per 100 nucleotides in all exons with a length between 101 and 150 nt, divided into groups based on exon inclusion levels.

C. Distribution of the number of enhancer-neutral ("E"/"N") state transitions per 100 nucleotides in all exons longer than 150 nt, divided into groups based on exon inclusion levels.

